



HAL
open science

Structural Influence on Exciton Migration and Singlet Oxygen Photosensitization in Porphyrinic Metal–Organic Coordination Networks

Paul Asselin, Adrien Schlachter, Daniel Fortin, Paul-Ludovic Karsenti, Pierre Harvey

► **To cite this version:**

Paul Asselin, Adrien Schlachter, Daniel Fortin, Paul-Ludovic Karsenti, Pierre Harvey. Structural Influence on Exciton Migration and Singlet Oxygen Photosensitization in Porphyrinic Metal–Organic Coordination Networks. *Chemistry of Materials*, 2022, 34 (16), pp.7242-7255. 10.1021/acs.chemmater.2c01105 . hal-04632369

HAL Id: hal-04632369

<https://hal.science/hal-04632369v1>

Submitted on 11 Sep 2024

HAL is a multi-disciplinary open access archive for the deposit and dissemination of scientific research documents, whether they are published or not. The documents may come from teaching and research institutions in France or abroad, or from public or private research centers.

L'archive ouverte pluridisciplinaire **HAL**, est destinée au dépôt et à la diffusion de documents scientifiques de niveau recherche, publiés ou non, émanant des établissements d'enseignement et de recherche français ou étrangers, des laboratoires publics ou privés.

Structural Influence on Exciton Migration and Singlet Oxygen Photosensitization in Porphyrinic Metal-Organic Coordination Networks

Paul Asselin,¹ Adrien Schlachter,¹ Daniel Fortin,¹ Paul-Ludovic Karsenti¹ and Pierre D. Harvey^{1}*

1- Département de Chimie, Université de Sherbrooke, 2500 Boul. de l'Université, Sherbrooke, (QC), J1K 2R1.

Keywords: Porphyrin, Metal-organic coordination network, Exciton migration, Singlet oxygen, Photosensitizer, Energy transfer.

Abstract: A hexagonal 3D metal-organic coordination network [(ZnTPyP) • 0.75 DMSO]_n (**3D Helix**) and a 1D coordination polymer [(ZnTPyP)•DMF]_n (**1D Ladder**) where ZnTPyP is 5,10,15,20-tetrakis(4-pyridyl)porphyrinatozinc(II), have been prepared and their photophysical properties were investigated to assess their ability to promote efficient exciton energy migration through singlet-singlet annihilation processes, and to photosensitize of singlet oxygen, ¹O_{2(g)}. The presence and absence of annihilation in **3D Helix** and **1D Ladder** respectively, proves indicative of their ability to efficiently promote exciton migration. Density functional theory (DFT) and time-dependant DFT (TDDFT) calculations were used to demonstrate the presence of inter-porphyrin couplings in the **3D Helix** structure. Using Forster's theory of energy transfer, the relative efficiencies of exciton migration across the bulk was corroborated by the structural parameter κ^2/r^6 where κ is an orientation factor related to the transition moments and r is the center-to-center distance between the energy donor and acceptor. Concurrently, based on the magnitude of ¹O_{2(g)} phosphorescence (1280 nm), it was noted that **3D Helix** photosensitizes ¹O_{2(g)} more efficiently than **1D Ladder** (by roughly one order of magnitude). During this study, a new 2D-MOCN was prepared, **2D Grid** [(ZnTPyP)•4CHCl₃]_n, but weak Zn···N interactions and evaporation of CHCl₃ transformed **2D Grid** into multiple phasic mixture (**ZnTPyP Morph**) containing both **3D Helix** and other 1D ladder-like species.

Introduction

Metal-organic frameworks (MOFs) are important materials for sustainable development and find applications in gas storage, compound separation,^{1,2} adsorption of organic and inorganic contaminants,^{3,4} depollution,⁵ energy,^{6,7} catalysis,⁸ antimicrobials,⁹ food packaging¹⁰ and photodynamic therapy,¹¹ to cite a few. These materials distinguish themselves by being constructed with metallic nodes and organic linkers forming porous 2D- and 3D-semiconducting frameworks, each playing active roles such as coordinating guest molecules, redox activities, and heavy atom effects on the excited state dynamics. The node is generally a polymetallic 0D- or 1D-secondary building unit (SBU). Concurrently, metal-organic coordination networks (MOCNs) are a subgroup of MOFs where the node consists of a single metal atom,¹² and porphyrins turn out to be ideal linkers for this subclass of materials.¹³⁻¹⁷ This versatile linker benefits from intense absorption bands in the visible region that allows porphyrin-based MOFs to perform well in fields such as photo-induced eradication of pollutants and toxins in water,¹⁸ photosensitization of singlet oxygen ($^1\text{O}_2$), for antibacterial and fungicidal purposes (in solution or from the air),¹⁹ photocatalytic transformation of organic molecules,²⁰ and cancer therapy.²¹ Concurrently, porphyrin-based MOCNs also exhibit rich visible light driven properties such as degradation of organic molecules and pollutants,²²⁻²⁸ organic synthesis,^{29,30} generation of solar fuels,^{31,32} and even solar cells.³³⁻⁴⁰ These photocatalytic and photo-sensitizing behaviors are profoundly influenced by the morphology of the solid,^{23,41,42} and also known to affect the nonlinear optical properties of solid samples.⁴³⁻⁴⁵ For instance, a direct link between excitation energy migration and up-conversion processes was recently established.⁴⁶

Porphyrins are efficient photosensitizers for the formation of singlet oxygen in MOFs¹⁸⁻²¹ and MOCNs,⁴¹ but its detection relies mainly on ESR spectroscopy (using spin traps) and

heterogeneous photocatalytic degradation of standard dyes in suspension in solution.¹⁹ These indirect methods only allow for qualitative assessments of performance as ESR is not a quantitative method and a suspension in solution still suffers from diffusion controlled processes in a liquid. Concurrently, the direct detection of $^1\text{O}_2(\text{g})$ at solid/gas interfaces from its phosphorescence in the near-IR region is more desirable, but proves to be quite rare as excitation usually requires a high intensity light source.⁴⁷⁻⁴⁹ Such a technique would provide a more reliable estimation of the relative production of $^1\text{O}_2(\text{g})$, and thus draw a direct link between the rate of excitation energy migration and the generation efficiency of $^1\text{O}_2(\text{g})$. This information would prove quite useful in assessing the performance of a new photocatalyst or photosensitizer reliably, particularly when structure and morphology vary from one sample to the next. We now report the photophysical traits, particularly the rates of excitation energy migration analyzed through the singlet-singlet annihilation process, and the phosphorescence of photosensitized $^1\text{O}_2(\text{g})$ at the solid-gas interface of two porphyrin-based MOCNs of 5,10,15,20-tetrakis(4-pyridyl)porphyrinatozinc(II) (ZnTPyP), referred to as **3D Helix** and **1D Ladder**. A heterogeneous mixture, **Morph**, arising from the rearrangement of a previously unknown **2D Grid** is also partially characterized. It is found that the **3D Helix** exhibits singlet-singlet annihilation when submitted to high intensity laser flux, indicating the presence of efficient excitation energy migration, whereas the **1D Helix** and the **Morph** mixture do not. Concurrently, the **3D Helix** photosensitizes significantly more $^1\text{O}_2(\text{g})$ than the **1D Ladder**, establishing for the first time a direct link between excitation energy migration and photosensitization efficiency of $^1\text{O}_2$.

Experimental section

All materials were purchased from Sigma-Aldrich and Oakwood Chemicals and used without further purification. DMF was dried over activated 3 or 4 Å molecular sieves.

Synthesis

H₂TPyP (adapted from ref⁵⁰): 4-pyridine carboxaldehyde (6.2 mL, 66 mmol) was added to N₂-saturated propionic acid (500 mL) and the mixture was heated to near-reflux under magnetic stirring and N₂ atmosphere. Pyrrole (4.6 mL, 67 mmol) was added over roughly 30 s. The mixture was shielded from light and brought to full reflux overnight. Once cooled to room temperature, the reaction mixture was chilled in the refrigerator overnight, and was Büchner-filtered under vacuum. The filtrate was diluted with an equal volume of cold water and filtered again directly on the purple solid again to catch more precipitate. The solid was rinsed with near boiling water followed by cold methanol (flasks should be changed to avoid flash-boiling the methanol) and dried *in situ*. The solid was dissolved in dichloromethane, the organic phase washed with water, dried with MgSO₄, and evaporated under reduced pressure. The residue was purified by flash chromatography on silica gel using CHCl₃:MeOH 3:1 as eluent. ¹H NMR confirmed identity and purity of the product (matte purple powder, yield = 32%). **¹H NMR (400 MHz, CDCl₃, δppm):** 9.07 (d, 8H); 8.87 (s, 8H), 8.17 (d, 8H); -2.92 (s, 2H).

ZnTPyP (adapted from ref⁵⁰): Pure H₂TPyP (255 mg, 0.41 mmol) was dissolved in a mixture of chloroform (1.9 mL) and methanol (0.5 mL) with zinc nitrate hexahydrate (360 mg, 1.65 mmol). The mixture was brought to reflux under magnetic stirring for 2 h. Once cooled to room temperature, the reaction mixture was washed with water. The organic phase was dried with MgSO₄ and evaporated under reduced pressure. The residue was purified by flash chromatography using CHCl₃:MeOH 4:1 as eluent. ¹H NMR confirmed identity and purity of the

product (metallic pinkish-purple powder, yield = 97%). **¹H NMR (Figure S1, 400 MHz, DMSO-d₆, δppm):** 9.03 (s, 8H); 8.85 (s, 8H), 8.24 (d, 8H).

3D Helix: A flame-dried 150 ml glass pressure vessel was loaded with H₂TPyP ligand (220 mg), zinc nitrate hexahydrate (1.492 g, 14 Eq) and dry DMF (40 mL). The flask was sonicated until homogeneous, sealed with a Teflon-lined cap, and heated in the oven at 100 °C for 23 h. After cooling to room temperature, the crystals were drained, rinsed with fresh dry DMF, and dried under vacuum. Boiling DMSO was poured on the crystals to recrystallize. The crystals were cooled to room temperature, vacuum-filtered and rinsed with a small amount of fresh DMSO, dried *in situ*, and subjected to moderate heat (approx. 60 °C) overnight. Structure elucidation was performed on a sufficiently large crystal. The powder XRD pattern matched the simulated one calculated from the elucidated X-ray structure, confirming the sample's homogeneity.

1D Ladder: ZnTPyP ligand (30.0 mg) was dissolved in dry DMF (8 mL) and nitrobenzene (0.1 mL). The mixture was sonicated 15 min in a sealed vial then and heated at 120°C for 24 h. After cooling to room temperature and decanting, DMF was drained, and the powder briefly rinsed in fresh dry DMF (1x 6 mL). The solvent was drained, and the powder dried under vacuum overnight. The powder XRD pattern matched the simulated one calculated from X-ray data, confirming the sample's homogeneity. Note that heating for 40 h instead of 24 h yielded the same structure.

2D Grid: ZnTPyP ligand (6 mg, 0.01 mmol) was dissolved in chloroform (4 mL) and nitrobenzene (1 mL). The vial was sonicated for 10 min and the mixture was left to evaporate slowly over 7 days at room temperature in a vibration-dampening sand bath with the screwcap loosely attached. Crystals were fished out of the solution and a XRD structure elucidation was

performed on a sufficiently large crystal. After several weeks, the powder XRD pattern no longer matched the simulated one calculated from the X-ray data indicating that this structure is metastable. The structure assignment of the various phases was performed (see phase analysis description below). Because of this meta-stability, only a partial characterization was performed.

Instrumentation and procedures

Nuclear magnetic resonance (NMR) spectra were recorded on a Bruker Advance 300 Ultrashield or Bruker AS400 NMR spectrometers. Chemical shifts are given in ppm relative to the residual peaks of CDCl_3 or DMSO-d_6 .

Thermogravimetric analysis (TGA) was performed on a Perkin-Elmer TGA 7 apparatus between 25 and 950 °C at 10 °C/min heating rate under argon atmosphere.

Infrared Spectra were recorded on an ABB Bomem MB104 series FTIR spectrometer with a resolution setting of 4 cm^{-1} . 128 scans were accumulated for both blank and sample acquisitions.

Solid-State UV-Vis absorption spectra were recorded on a Varian Cary 300 Bio UV-Vis spectrophotometer equipped with integration sphere using grazing angle transmittance or reflectance apparatus (298 K), or using a homemade low-temp reflectance sample holder (77 K). Samples were dispersed between two quartz plates.

Solution UV-Vis absorption spectra were recorded with an HP 8452A diode array spectrophotometer using 10x10 mm quartz cuvettes.

Solution and Solid-state UV-Vis emission and excitation spectra were acquired either on a Edinburgh Instruments FLS980 or a Horiba PTI QM-400, both equipped with Xe lamps and single-single monochromators. Samples were either dissolved in an appropriate solvent in 10x10 mm quartz cuvettes, introduced in a glass capillary, or dispersed between quartz plates. The spectra were corrected for instrument response.

Emission lifetime measurements were performed on the Edinburgh Instruments using a microchannel plate PMT and nano-LED lasers ($\lambda_{\text{ex}} = 395 \text{ nm}$; 15 mW; FWHM = 120 ns, or $\lambda_{\text{ex}} = 443 \text{ nm}$; 15 mW; FWHM = 120 ns). Measurements were performed using the time-correlated single-photon counting (TCSPC) method and data were treated by multi-exponential deconvolution analysis. All values are +/- 10%.

Singlet oxygen phosphorescence measurements were performed on the Horiba PTI QM-400 using a Hamamatsu PMT R5509-43 near-infrared photomultiplier tube (PMT) as detector. Samples were dispersed atop a quartz plate or borosilicate microscope slide and placed in an “open-sandwich” configuration in the sample holder. The plate has held vertically, at an angle of 38° relative to excitation beam, which may be adjusted to optimize the signal. A 335-610 nm bandpass filter (Thorlabs) was placed between the excitation monochromator and sample to filter stray light. A 715 nm or 1200 nm longpass filter (Newport) was placed between the sample and emission monochromator to filter harmonics and additional stray light capable of drowning out the $^1\text{O}_2$ signal. A diagram of the setup is provided in **Figure S15**. The data acquisition consists in an average of 5 to 20 scans with 1 to 2 s dwell time. The chromophore was excited in its most intense absorption band, *i.e.* the Soret band. Several data acquisitions were conducted first in air, followed by pure oxygen, then argon by purging the sample compartment. A rise and decrease of the signal at 1275-1280 nm were observed going from air to pure oxygen to argon, thus unambiguously demonstrating the presence of photosensitized singlet oxygen.

Singlet oxygen signal processing: Raw spectra were processed as little as possible to minimize any artificial impact on the signal. For **1D Ladder**, the oxygen and argon signal baselines were sufficiently similar for a simple subtraction. For **3D Helix**, the baselines from

each run were sufficiently offset from one another that a baseline correction was required. Details are given following **Figure S16**.

Powder X-ray diffraction (PXRD) was performed on a Bruker APEX DUO X-ray diffractometer. Samples were mixed with a small amount of paratone oil, cut to approx. $0.3 \times 0.3 \times 0.3 \text{ mm}^3$ and mounted on a sample holder cooled to 173.2 K. six correlated runs per samples with Phi Scan of 360 degrees and 270 s exposure time were collected with the Cu micro-focus anode (1.54184 Å) and CCD APEX II detector at a 150 mm distance. These runs from -12 to $-72^\circ 2\theta$ and 6 to 36° were then treated and integrated with the XRW2 Eval Bruker software to produce WAXD diffraction patterns from 2.5 to $82^\circ 2\theta$. The patterns were treated with Diffrac.Eva version 2.0 from Bruker.

Single-crystal X-ray diffraction (CXRD): The CXRD data of **3D Helix** and **2D Grid** are placed in **Tables S4 and S10**, respectively, in the Supporting Information.

Fast kinetic emission decay (“Power-dependence”) measurements: The laser source was the SHG of a Solstice (Spectra Physics) Ti-sapphire laser ($\lambda_{\text{ex}} = 398 \text{ nm}$; FWHM = 75-100 ps; 0.1 mJ per pulse; rep rate = 1 kHz; spot size B500 mm). The IRF became of a HWHM of 8 ps after passing through the optics. The detector was a Streak camera (Axis-TRS, Axis Photonique Inc.) with typically less than 8 ps resolution. Samples were dispersed between two quartz plates or introduced in a capillary. The results were globally analysed with Glotaran (<https://www.glotaran.org>) allowing for the extraction of a sum of independent exponentials: $I(\lambda, t) = C_1(\lambda)\exp(-t/\tau_1) + C_2(\lambda)\exp(-t/\tau_2) + C_3(\lambda)\exp(-t/\tau_3) + \dots$

Computations: All Density Functional Theory (DFT) and time-dependent (TD-DFT) were performed with Gaussian 16⁵¹ at *Université de Sherbrooke* on the *Mammoth* supercomputer supported by *Calcul Québec*. X-ray crystal structure of **3D Helix** was used for the calculations.

The DFT (singlet single-point energy (SPE) and triplet optimization) and TD-DFT⁵²⁻⁶¹ calculations were carried out using the B3LYP method, using 6-31g(d,p) basis set for C, H, and N atoms.⁶¹ VDZ (valence double ζ) with SBKJC effective core potential were used for all Zn atoms.⁶²⁻⁶⁷ The calculated electronic absorption spectra were obtained using Gauss Sum 3.0.⁶⁸

Phase analysis of Morph: The experimental PXRD pattern was blindly compared to the simulated ones of all crystal structures of ZnTPyP in the literature. The simulated patterns were then shortlisted, and different combinations were analyzed to account for as many major peaks of the experimental pattern as possible, using as many major peaks of each simulated patterns as possible. See **Figures 13** and **S11** for details.

Results and Discussion

Auto-assembly of ZnTPyP: ZnTPyP may crystallize in five metal-organic coordination networks (**Figure 1**): 1D single zig-zag chain,^{69,70} 1D double zig-zag chain,^{69,71,72} 1D ladder chain (such as **1D Ladder**),^{70,73-75} 2D-grid (such as **2D Grid**),^{72,76} or 3D hexagonal and porous network (such as **3D Helix**).^{69,72,77-81}

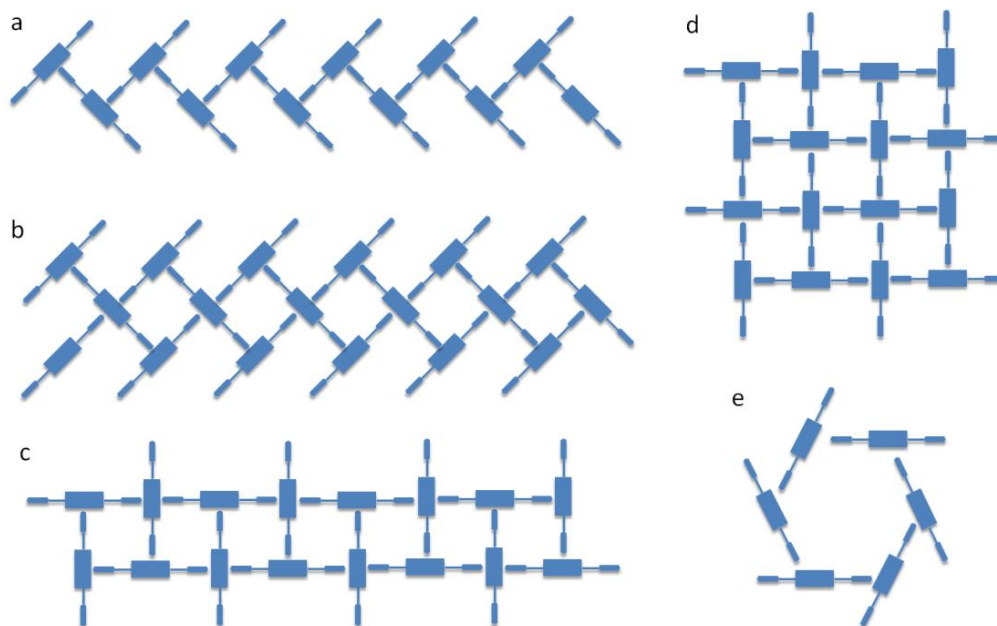



Figure 1: Known topologies of ZnTPyP MOCNs: a) 1D single zig-zag chain; b) 1D double zig-zag chain; c) 1D Ladder chain (such as **1D Ladder**); d) 2D Grid (such as **2D Grid**); e) 3D hexagonal network (such as **3D Helix**); ZnTPyP = .

Two of them, 1D ladder chain (**1D Ladder**, low-dimensionality and less porous) and hexagonal network (**3D Helix**, high-dimensionality and more porous), were selected to compare the properties of two dramatically different MOCNs.

3D Helix

The synthetic procedure used herein differs from the previous ones^{69,72,77-81} and involves two steps: first, solvothermal synthesis in DMF, followed by a recrystallization from boiling DMSO, which afforded crystals of suitable quality of X-ray structure analysis. The X-ray data revealed the 3D-helix structure, which matched the previously reported structures (**Figure 2**).^{69,72,77-81} The difference is that DMSO molecules are found inside the pores of the networks and these molecules were not removed in this investigation. Indeed, the IR spectra exhibit $\nu(\text{C-H})$, $\nu(\text{C=N})$ and $\nu(\text{C=C})$ peaks expected for the ligand but also a strong $\nu(\text{S=O})$ and a broad $\nu(\text{O-H})$ bands at ~ 1000 and $\sim 3400 \text{ cm}^{-1}$, respectively, indicative of DMSO and water (**Figure S3**). The presence of water is also corroborated by TGA where a weight loss is depicted in the vicinity of 100°C as well as DMSO with a weight loss starting around 190°C (**Figure 2**). To confirm that the powdery samples exhibit the same network phase as for the crystal, the powder XRD pattern was compared to that calculated from the CXRD (**Figure 2**).

Thermogravimetric analysis: The two first weight losses (20-200 °C range) are attributed to water and then DMSO evaporation. The third weight loss (300-600 °C) is attributed to the loss of 1 non-coordinating pyridine. The fourth weight loss (600+ °C) is also attributed to the loss of

another non-coordinating pyridine (**Figure 2** and **Table S2**). *Elemental analysis* (CHN) also corroborated the composition of the sample (**Table S3**).

X-ray structure: The crystal structure of the **3D Helix** was confirmed by single crystal X-ray diffraction (**Figure 2**) but differs from the literature as it contains 0.76 DMSO molecule per ZnTPyP unit, which is found to be disordered in the lattice. The porosity of this structure has been confirmed by BET analysis reported for a similar 3D Helix.⁸² It is noteworthy that brief sonication of the solid sample (5 min) results in decomposition.

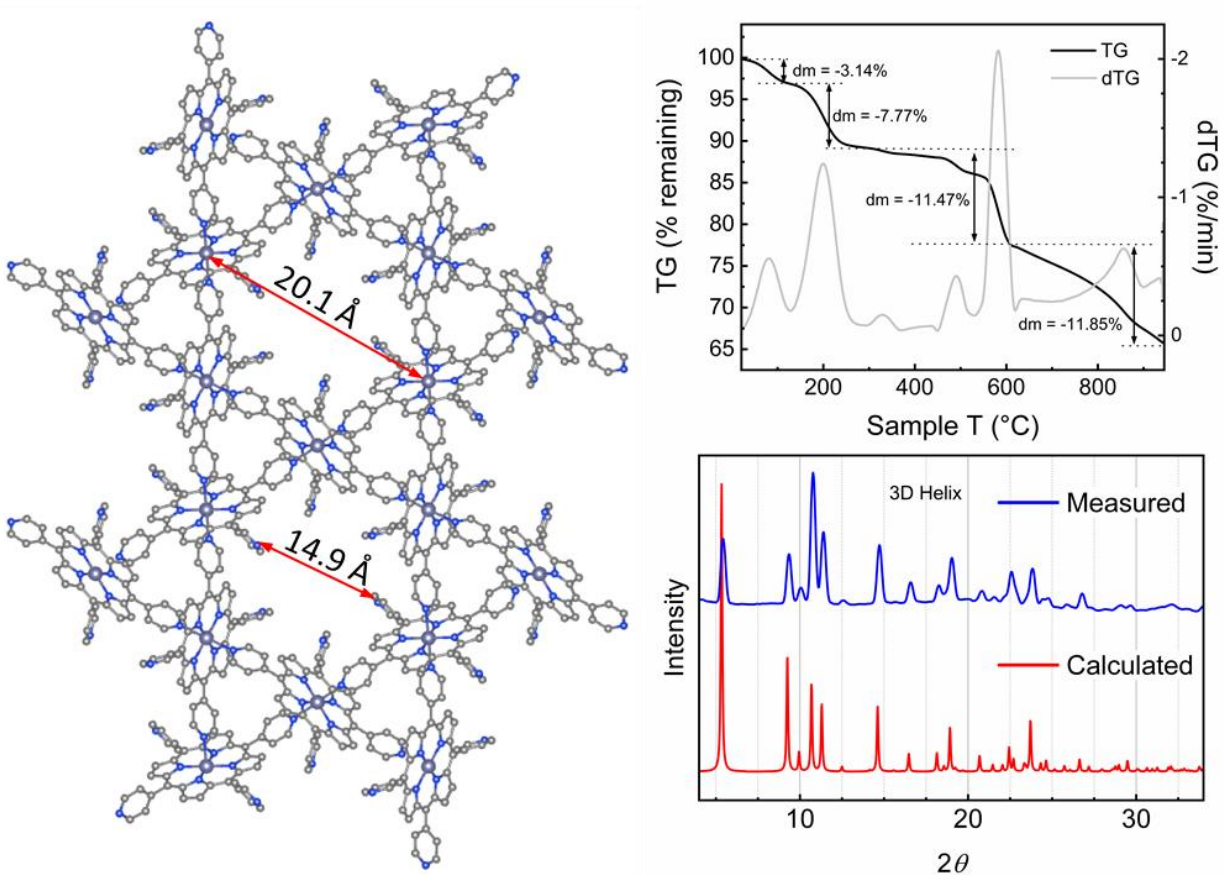


Figure 2: Structure (left; solvent molecules and hydrogens have been omitted for clarity), TGA traces (black) and 1st derivative (grey; top right), and comparison of simulated and experimental PXRD patterns (bottom right) of **3D Helix**.

Absorption spectra and DFT calculations: Absorption spectra of ZnTPyP in solution⁸³ and as thin films^{84,85} are reported in the literature, but to the best of our knowledge, not as a bulk sample. Reflectance absorption spectra at 298 and 77 K are presented in **Figure 3**. Both Soret and Q-bands appear broader than in thin films,^{84,85} and significant band splitting (4 bands and a shoulder) is observed, most likely due to exciton coupling.⁸⁶ This feature along with the description of the frontier MOs are addressed by DFT calculations. The representation of the frontier orbitals of **3D Helix** is given in **Figure 4**. The key takeaway here is that these MOs are quasi-degenerated and spread out over several units. These computational results support the exciton splitting explanation of the experimental spectra. Further TDDFT computations indicate that a total of 100 spin-allowed electronic transitions ($S_0 \rightarrow S_n$) within 127 nm of the lowest energy transitions (**Table 1**, **Table S5**). These results concur with the large width of the experimentally observed absorption bands. Furthermore, each $S_0 \rightarrow S_n$ transition is fed by several individual orbital-to-orbital transitions of the appropriate energies, indicating that singlet excited states are heavily mixed, which is also consistent with the presence of exciton coupling. This coupling is likely to efficiently promote energy migration across the solid structure.

Emission spectra and lifetimes: Emission of the 3D-Helix consists in a broad fluorescence double-band centered at roughly 700 nm, and a phosphorescence peak at 766 nm (**Figure 3**). The breadth of these bands contrasts with those of isolated chromophores, further confirming the bulk effect on electronic properties and exciton coupling. Conversely, the phosphorescence band is much narrower and reminiscent of ZnTPyP in solution.⁸⁷ This sharp signal indicates absence of exciton coupling in the triplet state. This observation is corroborated by the HSOMO and LSOMO profiles; each being highly localized on single porphyrin units (**Figure 4**).

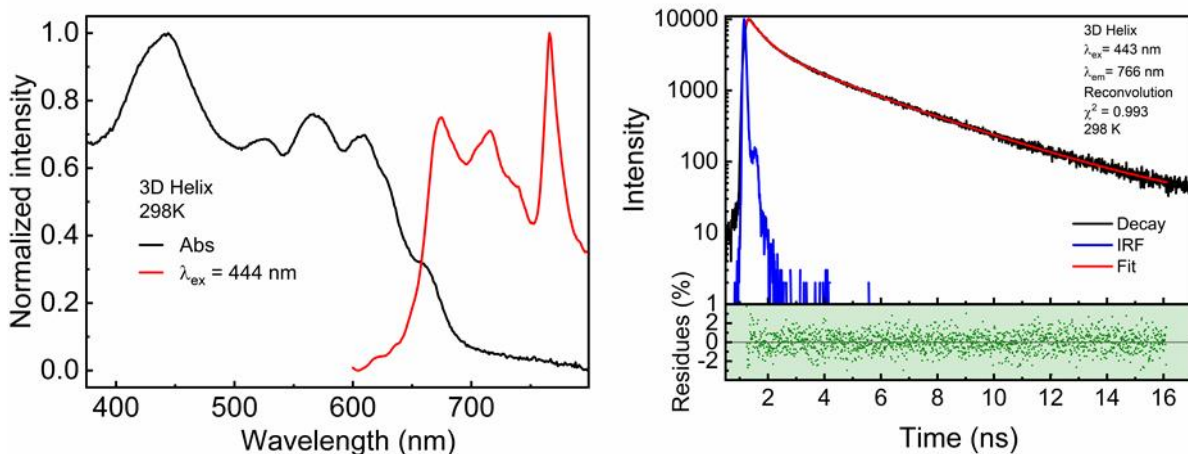


Figure 3: Left: Absorbance (black) and emission (red) spectra of **3D Helix** at 298 K. Right: emission decay (black), fit (red), IRF (blue) and residues (green) of **3D Helix** at 298 K. Three-component decay: $\tau_1 = 0.41$ ns (17%, $B_1 = 0.0589$); $\tau_2 = 1.16$ ns (19%, $B_2 = 0.0227$); $\tau_3 = 3.25$ ns (64%, $B_3 = 0.0278$). All values $\pm 10\%$. Spectra and decay measured at 77 K are provided in **Figure S4**.

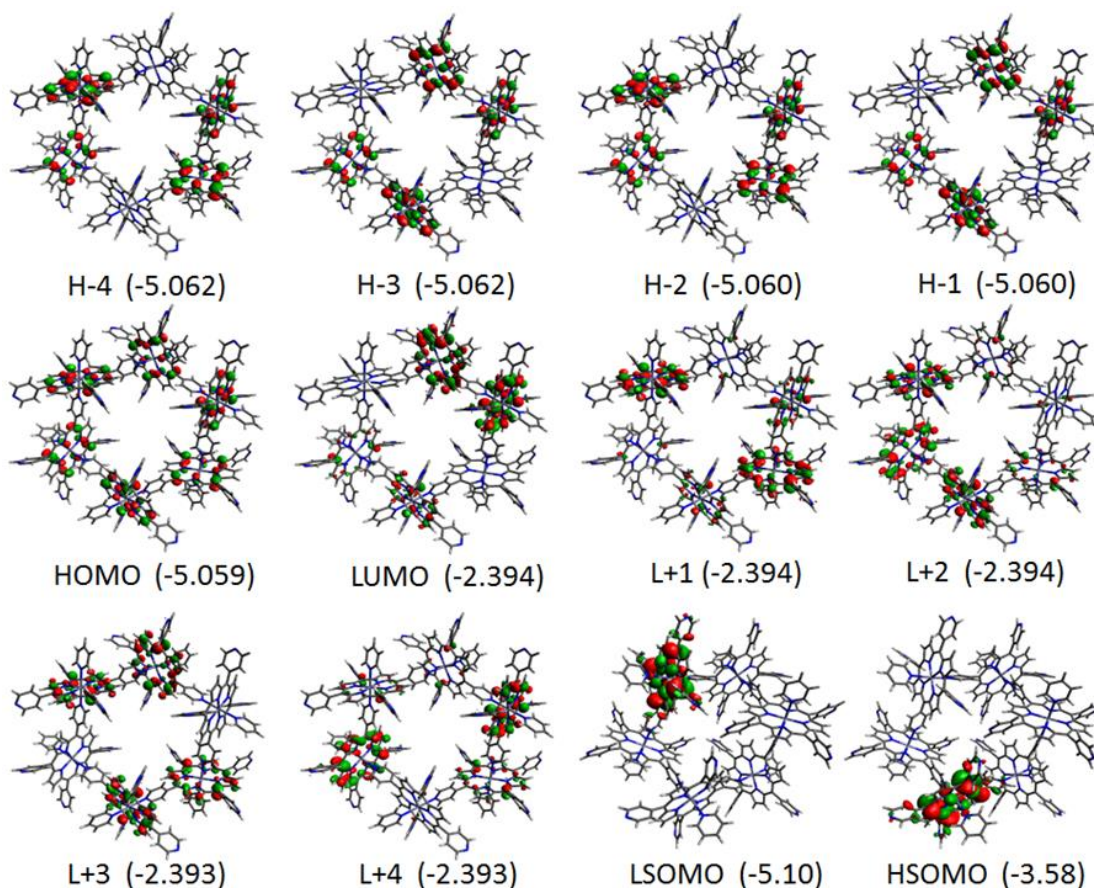


Figure 4: The frontier MOs of **3D Helix**. (H = HOMO, L = LUMO, LSOMO = low single-occupied MO, HSOMO = high single-occupied MO). Energies are in eV.

The solid-state emission decays are triphasic with one component in the low ps range and two others in the low ns range (**Figure 3, Table 2**). In dilute conditions (DMSO) at room temperature, τ_{Fluo} is found to be ~ 1.6 ns (TCSPC), while the triplet state does not seem accessible, and no phosphorescence band is observed, though triplet lifetime has been reported using laser induced optoacoustic spectroscopy (~ 500 ns, very dilute in CHCl_3 at 298 K).⁸³ Based on this, it is possible to assign the two faster components, 0.41 (minor) and ~ 1.2 ns (major), to fluorescence and the slower component (~ 3.2 ns) to phosphorescence. This latter component is much shorter than 500 ns suggesting that the solid-state packing influences significantly the triplet state

dynamic. The presence of two components for the fluorescence decay indicates the presence of two emissive sites, presumably surface and bulk portions of the microcrystals.

Table 1: Calculated positions, oscillator strengths (f) and major contributions of the first 5 electronic transitions in **3D Helix** (first 100 transitions in **Table S5**).

#	λ (nm)	f	Major contributions (%) (7% and over)
1	558.3	0.0653	H-3→L+5 (11), HOMO→LUMO (10), H-1→L+2 (9), H-5→L+3 (7)
2	558.3	0.0656	H-4→L+5 (11), HOMO→L+1 (10), H-2→L+2 (9), H-5→L+4 (7)
3	558.3	0.0009	H-1→L+5 (11), H-3→L+2 (9), HOMO→L+3 (9), H-5→LUMO (8)
4	558.2	0.0009	H-2→L+5 (11), H-4→L+2 (9), HOMO→L+4 (9), H-5→L+1 (8)
5	557.8	0.0002	H-5→L+5 (11), H-2→L+1 (10), H-1→LUMO (9), HOMO→L+2 (9), H-4→L+4 (7), H-3→L+3 (7)

Table 2: Fluorescence lifetimes of ZnTPyP Monomer, **3D Helix**, **1D Ladder**, and **Morph**.

Structure	τ_e (ns) ^a (f (%)) ^{b,c}			χ^2
	Component 1 (fluorescence)	Component 2 (fluorescence)	Component 3 (phosphorescence)	
Monomer (DMSO) 298 K	-	1.59 (100)	-	1.03
3D Helix , 298 K	0.41 (17.0)	1.17 (18.9)	3.25 (64.1)	0.99
3D Helix , 77 K	0.45 (6.0)	1.34 (18.7)	3.29 (75.3)	1.03
1D Ladder , 298 K	0.36 (48.9)	0.79 (51.1)	-	1.00
1D Ladder , 77 K	0.65 (41.2)	1.78 (58.8)	-	1.10
Morph , 298 K	0.02 (28.3) ^c	0.56 (71.7)	-	1.02

^a TCSPC. Uncertainties are $\pm 10\%$ on all measurements. ^b f_i (%) = $(B_i\tau_i)/\Sigma(B_i\tau_i)$; $I_e = B_1 \exp(-t/\tau_1) + B_2 \exp(-t/\tau_2) + \dots$ ^c The full-width at half maximum (FWHM) of the nanodiode laser is ~ 120 ps. Any value smaller than 120 ps (0.12 ns) should not be considered precise.

Singlet-singlet annihilation: The fluorescence intensity of **3D-Helix** expectedly increases with the excitation flux. This increase is not linearly respective to the power, but rather is linear to the square-root of excitation power, $(\text{Power})^{1/2}$ (**Figure 5a**). This behavior is due to singlet-singlet annihilation ($S_1 + S_1 \rightarrow S_n + S_0 + \text{heat}$; then $S_n \rightsquigarrow S_1 (+ \text{heat}) \rightarrow S_0 + h\nu$), as two absorbed photons yield less than two emitted photons due to a partial loss of energy (heat). Both singlet emission lifetimes, τ_1 and τ_2 , decrease as a function of the excitation flux (power or $(\text{power})^{1/2}$; **Figure 5b**), which is fully consistent with excited state quenching ($S_1 + S_1 \rightarrow S_n + S_0$).

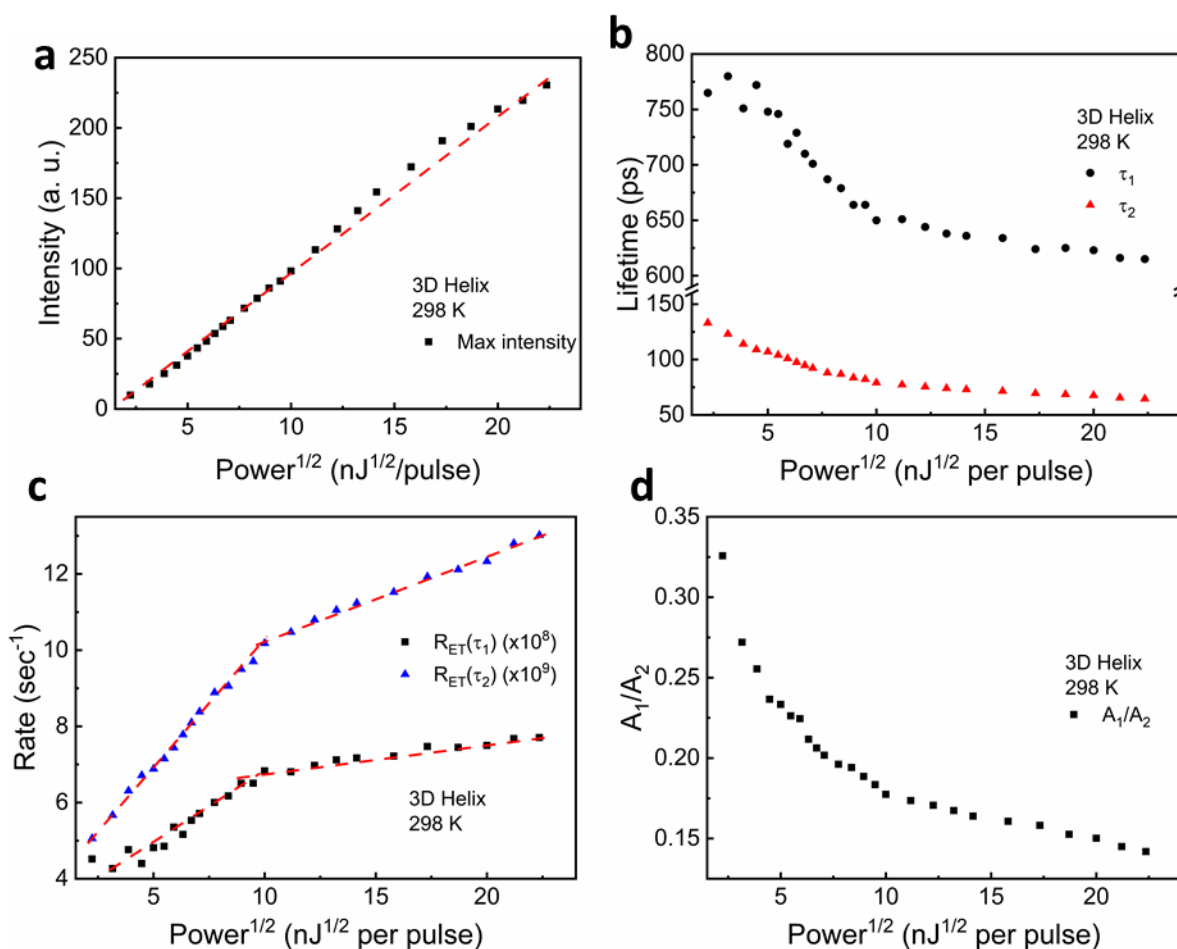


Figure 5: Power-dependence measurements on **3D Helix** at 298 K. **a:** graph reporting emission intensity as a function of $(\text{Power})^{1/2}$. **b:** change in emission lifetimes as a function of $(\text{Power})^{1/2}$. **c:**

deactivation rates of the two emission decays vs $(\text{Power})^{1/2}$. **d**: ratio of A_1/A_2 as a function of $(\text{Power})^{1/2}$. The 77K data is presented in **Figures S5** and **S6**.

The quenching rates (k_Q 's) are evaluated by $k_Q = ((1/\tau_e) - (1/\tau_e^\circ))$ where τ_e and τ_e° are the emission lifetime in the presence and absence of quenching, respectively. The τ_e° values are those measured by TCSPC where a light source is of minimal power. These rates plotted against $(\text{Power})^{1/2}$ increase in a linear fashion (**Figure 5c**), which is consistent with the increasing number of excitons in the bulk. However, a drastic change in increase of rates vs $(\text{Power})^{1/2}$ is noted at $\sim 10 \text{ nJ}^{1/2}$ for both components where the rates do not increase as fast at higher excitation flux. This behavior is associated with saturation in a process leaving the other process to operate alone (somewhat like a bottleneck effect). This feature becomes evident when observing the pre-exponential factors for each component (A_1 for τ_1 , and A_2 for τ_2). The A_1/A_2 ratio decreases gradually with $(\text{Power})^{1/2}$ (**Figure 5d**) meaning that component 1 becomes less operative relative to component 2. The behavior changes at $\sim 10 \text{ nJ}^{1/2}$ where the A_1/A_2 ratio decreases linearly with $(\text{Power})^{1/2}$. The phosphorescence component was not investigated since the 3 ns component falls outside the detection range of the instrument.

In order to provide an interpretation to the results, the data was analyzed in terms of the Forster theory of energy transfer. The exciton migration from one chromophore to the next in the bulk proceeds through energy transfer ($S_1 + S_0 \leftrightarrow S_0 + S_1$) and straight-line directions are generally the paths that are the most efficient for energy delocalization. Two examples of paths (blue and red arrows) are shown in **Figure 6**. These paths may or may not include the -pyridine-Zn-pyridine-Zn-linkage-, which correspond to “through bond” (red path) and “through space” (blue path) processes, respectively. A total of three paths were clearly identified based on the 3D-crystal structure (**Figure 7**).

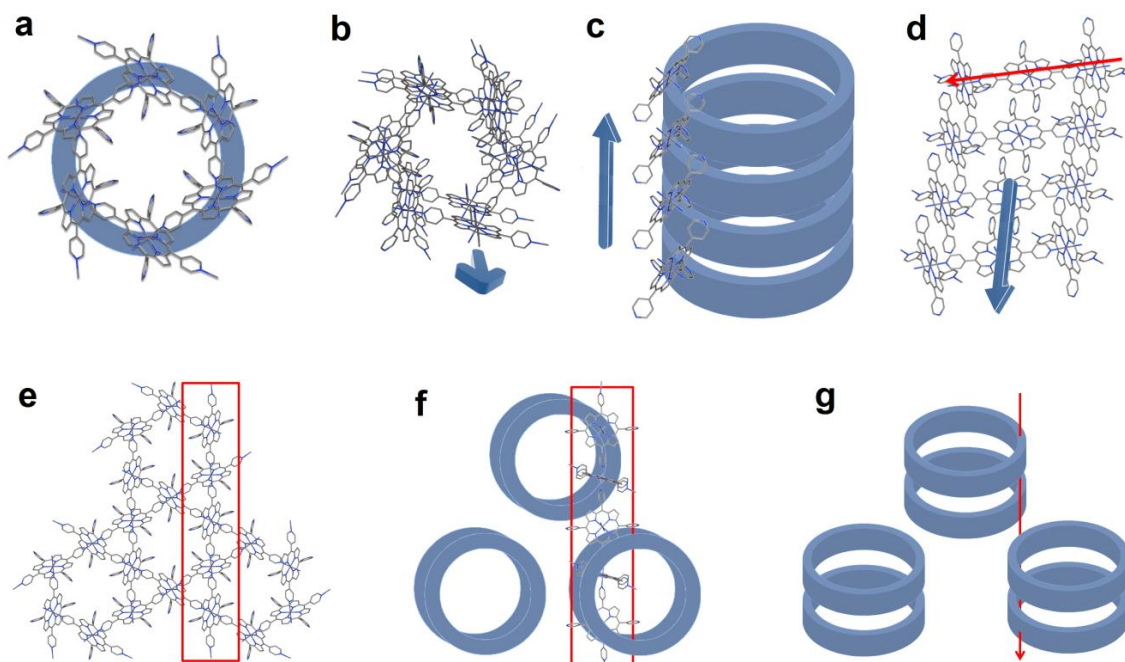


Figure 6: Hexagonal structure of **3D Helix** with linear $(\text{ZnTPyP})_n$ patterns: (a) Visualization of a hexagonal $(\text{ZnTPyP})_6$ unit with a ring. (b)-(d) Three different perspectives showing the stacking of the hexagonal units where the blue arrows show a possible pathway for exciton migration (path C, through space). (e)-(g) Another possible path for migration (red rectangle or arrow; path A, through coordination bonds).

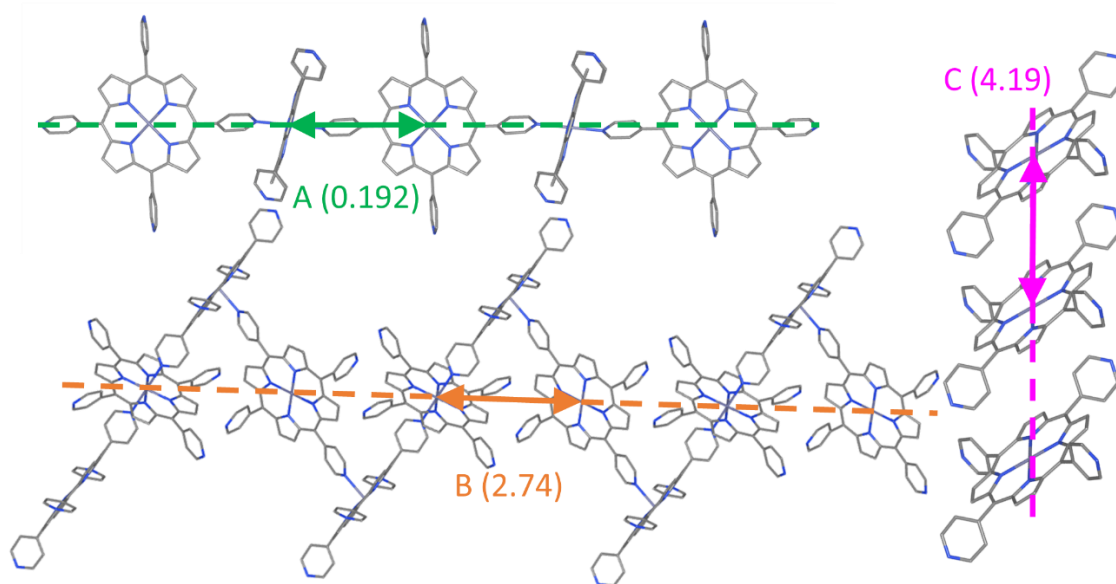


Figure 7: Three possible paths for exciton migration in **3D Helix**. A) (green): through N-Zn-N coordination bonds; B) (orange) and C) (purple): through space and their respective κ^2/r^6 ($\times 10^{-7}$ \AA^{-6}) parameters.

Assigning paths to quenching processes: Quenching occurs when two excitons meet and these excitons migrate at various speeds according to their paths, and thus as a function of the relative geometry and distance of the two interacting chromophores according to the Förster theory of energy transfer,^{88,89} in this case: $S_1 + S_0 \leftrightarrow S_0 + S_1$. The rate of singlet energy transfer is given by using eq (1):⁹⁰⁻⁹²

$$k_{ET} = \frac{\Phi_{F^{\circ}}(D)\kappa^2}{\tau_{F^{\circ}}r^6} \left(\frac{9000(\ln 10)}{128\pi^5 n^4 N_A} \right) \frac{\int F_D(\lambda)\epsilon_A(\lambda)\lambda^4 d\lambda}{\int F_D(\lambda)d\lambda} \quad (1)$$

Where $\Phi_{F^{\circ}}(D)$ and $\tau_{F^{\circ}}(D)$ are respectively the fluorescence quantum yield and lifetime of the donor (D) in the absence of energy transfer (*i.e.* unimolecular radiative rate constant, $k_{F^{\circ}} = \Phi_{F^{\circ}} / \tau_{F^{\circ}}$), κ^2 is the orientation factor between donor and acceptor (as described by eqs (2) and (3) below), r^6 is the center-to-center distance between the donor and acceptor, n is the refractive index, N_A is the Avogadro's number, F_D is the normalized fluorescence intensity of the donor, and ϵ_A is the molar extinction coefficient of the acceptor. The orientation factor κ^2 is calculated by the following eqs:

$$\kappa(\nu) = \cos \varphi - (3 \cos \theta_D \cos \theta_A) \quad (2)$$

$$\kappa^2 = \frac{(|\kappa(\nu)| + |\kappa(\nu + \pi/2)|)^2}{4} \quad (3)$$

Where φ is the dihedral angle between the planes of the donor and acceptor and θ_D and θ_A are the angles made by the transition moments of porphyrin (*i.e.* along the N-Zn-N axes) relative to the center-to-center axis (Zn \cdots Zn). Note that eq 3 is needed because of the degenerated nature of the transition moments as the point group of ZnTPyP is D_{4h} . The only variables in the context of

this study are κ^2 and r^6 (all other are characteristic of ZnTPyP and can be approximated as unchanging), so that k_{ET} is directly proportional to the ratio κ^2/r^6 . Consequently, this ratio is sufficient to qualitatively assign paths to quenching rates. r^6 is evaluated by measuring the Zn...Zn distances between two adjacent porphyrins in the crystal (**Figure 7**). The angles are also extracted from the crystal data. The two N-Zn-N axes are considered in equation (3) with $\kappa(v)$ and $\kappa(v+\pi/2)$ which represent them and their 90° offset relative to each-other. Two porphyrins with two possible θ_D and θ_A means four possible κ values, which implies that each combination must be calculated and averaged for a final orientation factor κ^2 (**Table 3**). The individual κ values are placed in **Figure 7** and **Table S6**. These averaged κ^2/r^6 values can be separated into two categories: small ($1.92 \times 10^{-8} \text{ \AA}^{-6}$) and large (2.74×10^{-7} and $4.19 \times 10^{-7} \text{ \AA}^{-6}$) respectively leading to a slow and fast k_{ET} , the two large values being in the same order of magnitude. It becomes apparent that path A (through bond) is associated with a slow rate ($R(\tau_1)$) while paths B and C (through space) are experimentally indistinguishable and are associated with a fast rate ($R(\tau_2)$) of singlet-singlet annihilation (**Figure 5c**). At 77 K, the same trend is observed with a small difference: the saturation point occurs near $8 \text{ nJ}^{1/2}$. In all, **3D Helix** provided clear evidence for exciton energy migration across the crystal.

Table 3: Calculated FRET factors for **3D Helix** exciton migration paths.^a

Path ^b	Averaged κ^2	$r \text{ (\AA)}^c / r^6 \text{ (\AA}^6)$	Averaged $\kappa^2/r^6 \text{ (\AA}^{-6})$
A	0.02	10.05 / 1.03×10^6	1.92×10^{-8}
B	0.60	11.40 / 2.19×10^6	2.74×10^{-7}
C	0.28	9.35 / 6.64×10^5	4.19×10^{-7}

^a Distances and angles were extracted from the respective CIF files using the Mercury software package from the Cambridge Crystallographic Data Center (CCDC). ^b These paths refers to

Figure 7. c is the Zn...Zn distance between one porphyrin and the next in the path. Details are provided in **Table S6**.

1D Ladder

1D Ladder was determined to have the formula $[(ZnTPyP) \cdot DMF]_n$. The synthetic procedure described in the Experimental Section represents a significant improvement compared to the ones previously reported (a fast biphasic synthesis⁷⁰ or a slow monophasic⁹³ one). Its characterization of the resulting powder is shown in **Figure 8** (TGA, PXRD), **Figure S7** (IR), **Table S7** (TGA) and elemental analysis (**Table S8**). The experimental PXRD pattern matches that of the simulated one extracted for the single crystal data structure (**Figure 8**).

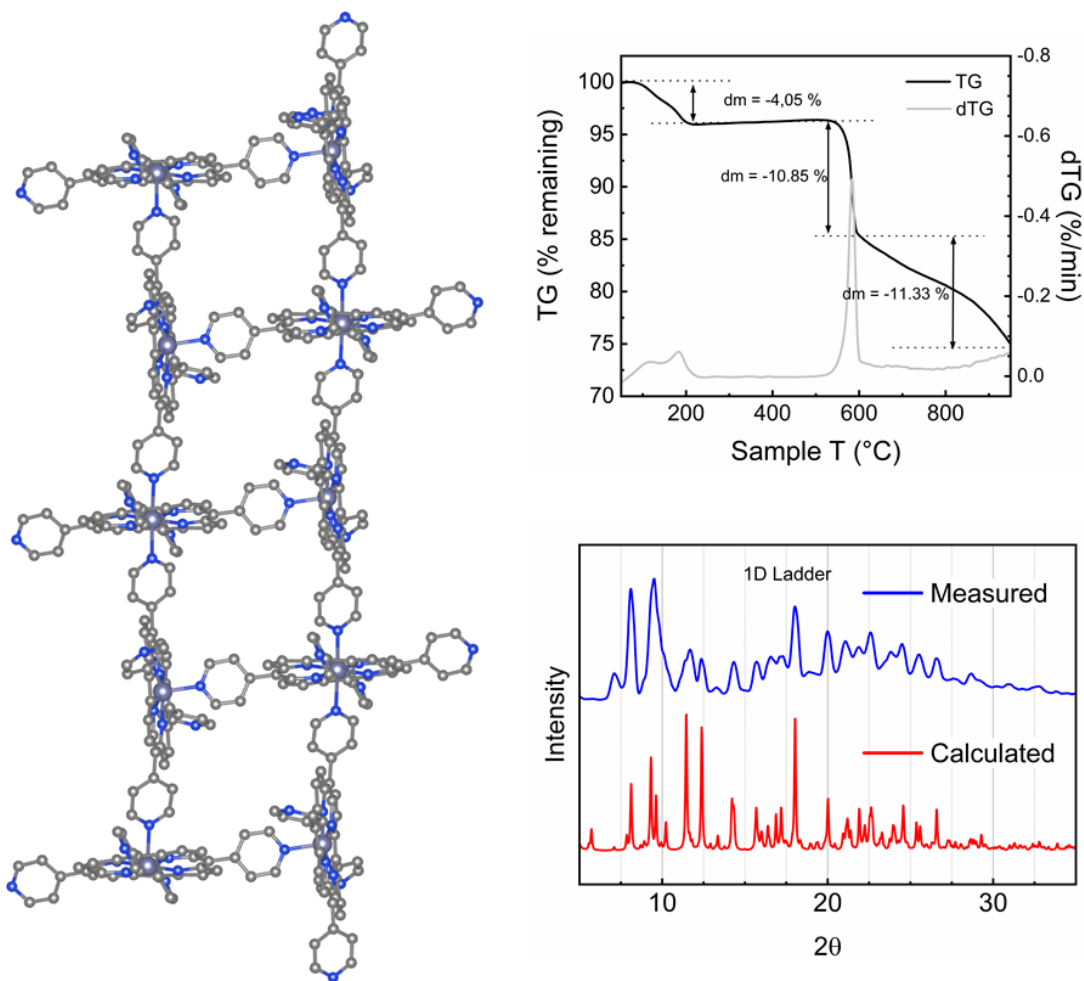


Figure 8: Left: structure of **1D Ladder** (Solvent molecules and hydrogens have been omitted for clarity). Top right: TGA trace (black) and its first derivative (grey). Bottom right: comparison of the simulated and experimental PXRD patterns of **1D Ladder** demonstrating the presence of a pure phase.

Thermogravimetric analysis: The first two weight losses in the 150-200°C range are attributed to water and DMF evaporation (or decomposition). The third and rapid weight loss is attributed to the loss of 1 pyridine. The fourth weight loss is also attributed to the loss of another pyridine. The slow rate of weight losses may be attributed to temperature-induced morphological changes hindering vaporization, as well as slow pyrolysis of the remaining structure. This proposal is based on the existence of many reported X-ray structures for ZnTPyP-based MOCNs in **Figure 1**, and the new structure described below.

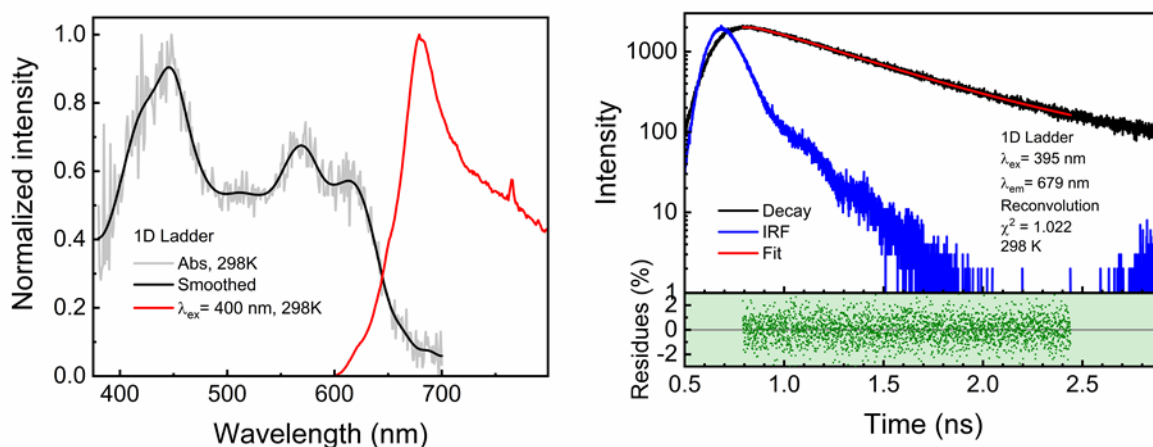


Figure 9: Left: absorbance and fluorescence spectra of **1D Ladder** at 298 K. Right: fluorescence decay (black), fit (red), IRF (blue) and residual (green) of **1D Ladder** at 298 K. Two-component decay: $\tau_1 = 0.37$ ns (49%, $B_1 = 0.0031$); $\tau_2 = 0.79$ ns (51%, $B_2 = 0.0015$). All values are $\pm 10\%$. 77 K measurements are presented in **Figure S8**.

Absorption and fluorescence spectra and lifetime: The absorption and emission spectra of **1D Ladder** exhibit significantly different signatures from those of **3D Helix** (**Figure 9**). The Q-band region exhibits three bands (instead 4 bands and a shoulder) suggesting that exciton coupling is less apparent. This difference in band-shape is also depicted in the fluorescence spectra, and in the emission decay. Note that at 77 K, the spectra become more resolved (SI). The decay is also described by a double exponential ($\tau_e = 0.36$ and 0.79 ns; both components are assigned to fluorescence) at 298 K, which differ from the triphasic decay of **3D Helix**, which also include an additional phosphorescence component.

Singlet-singlet annihilation: As the flux of photons increases, the fluorescence increases linearly with excitation power (**Figure 10** (left) and **Figure S9**). A graph reporting the non-linear relationship of the fluorescence intensity with $(\text{Power})^{1/2}$ is presented in **Figure S9**. This behavior indicates absence of singlet-singlet annihilation in **1D Ladder**. This fact is corroborated the absence of quenching detected by the absence of change of the fluorescence lifetime with the excitation power (**Figure 10** (right)). To explain the absence or inefficiency of exciton energy migration, the six possible intrachain paths were examined (**Figure 11**) and the κ^2 , r^6 and κ^2/r^6 parameters have been summarized in **Table 4** (detailed analysis in **Table S9**).

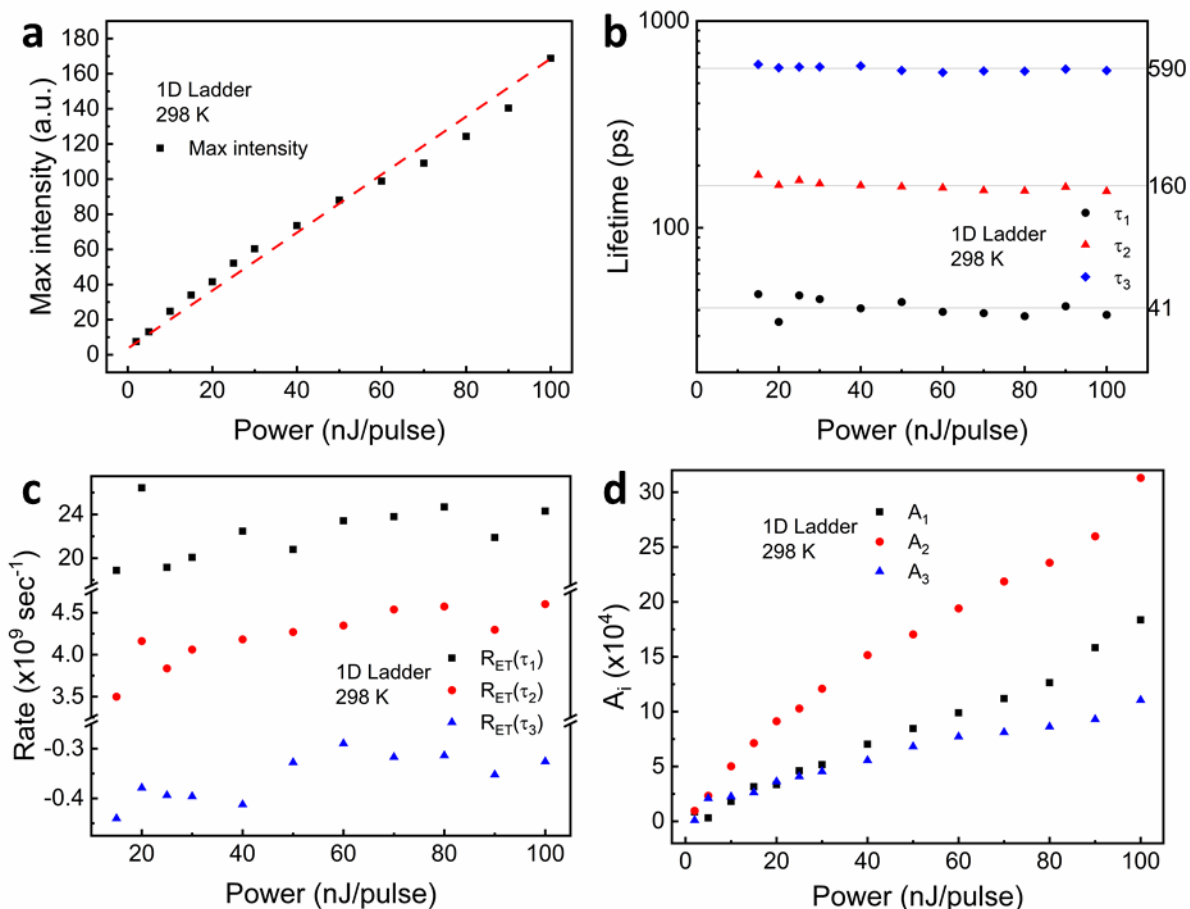


Figure 10: Power-dependence of the fluorescence intensity and lifetimes of **1D Ladder** at 298 K. **a:** emission intensity as a function of power. **b:** emission lifetimes remain relatively constant as a function of power. **c:** deactivation rates of emission decays vs power. **d:** pre-exponential factors A_i as a function of power. Behaviors presented here do not change at 77 K (**Figures S9 and S10**). Note the presence of the very short-lived component (< 100 ps) undetected by the TCSPC system as FWHM of the excitation pulse is 120 ps.

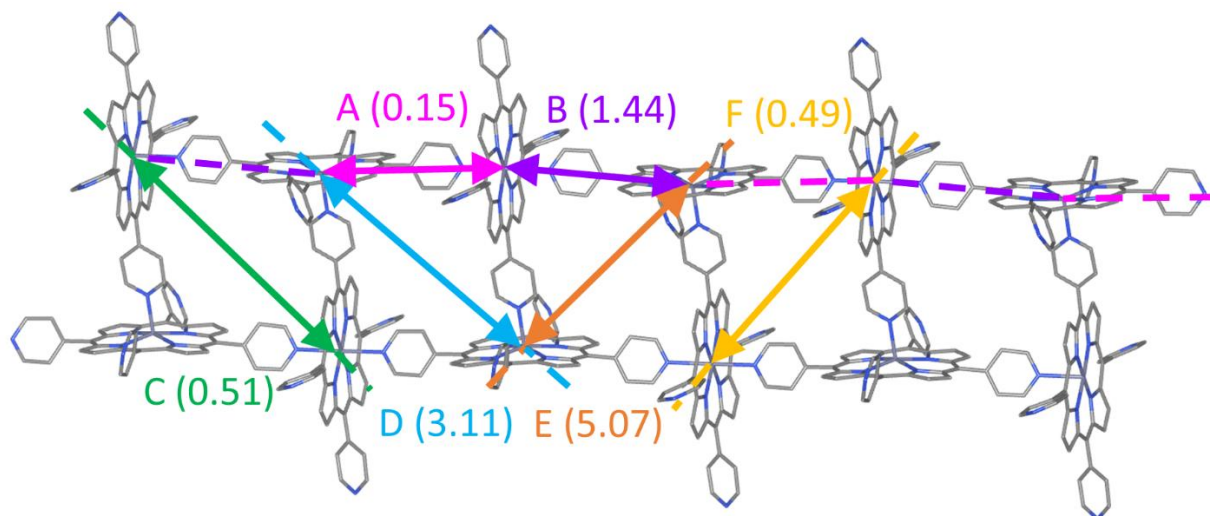


Figure 11: All 6 possible exciton migration paths in **1D Ladder** and their respective averaged κ^2/r^6 ($\times 10^{-8} \text{ \AA}^{-6}$) parameters; through bond: A (pink) and B (purple); through space: C (green), D (blue), E (orange), F (yellow). Zn-Zn distances are 9.99, 10.20, 15.32, 14.26, 12.92 and 13.79 \AA .

Table 4: Calculated FRET factors for **1D Ladder** exciton migration paths.^a

Path	Averaged κ^2	r (\AA) ^b / r^6 (\AA^6)	Averaged κ^2/r^6 (\AA^{-6})
A	0.0015	9.996 / 9.98×10^5	0.15×10^{-8}
B	0.0163	10.201 / 1.13×10^6	1.44×10^{-8}
C	0.0674	15.322 / 1.27×10^7	0.51×10^{-8}
D	0.2610	14.256 / 8.39×10^6	3.11×10^{-8}
E	0.2361	12.924 / 4.66×10^6	5.07×10^{-8}
F	0.0339	13.795 / 6.89×10^6	0.49×10^{-8}

^a Distances and angles were taken from the CIF file using the Mercury software package from the Cambridge Crystallographic Data Center (CCDC). ^b r is the Zn \cdots Zn distance between one porphyrin and the next in the path.

For **3D Helix**, the linear through bond path A has an averaged κ^2/r^6 of $1.92 \times 10^{-8} \text{ \AA}^{-6}$ and is considered the slow path. This situation indicates any $\kappa^2/r^6 < 1.92 \times 10^{-8} \text{ \AA}^{-6}$ would lead to even

slower exciton migration. The corresponding linear path for the **1D Ladder** proceeds as (path A + path B)_n with two distinct averaged κ^2/r^6 ratios: 0.15×10^{-8} and $1.44 \times 10^{-8} \text{ \AA}^{-6}$, both being smaller than that for **3D Helix**'s $1.92 \times 10^{-8} \text{ \AA}^{-6}$. Because quenching cannot occur faster than the determining step (*i.e.* the slower $0.15 \times 10^{-8} \text{ \AA}^{-6}$), then the rate of exciton energy migration along the (path A + path B)_n in **1D Ladder** is structurally slower than the of corresponding path A in **3D Helix** (averaged κ^2/r^6 ratio of $1.92 \times 10^{-8} \text{ \AA}^{-6}$) by at least an order of magnitude. Singlet-singlet annihilation appears quite difficult in this case and would explain the lack of symptoms of this phenomenon in **1D Ladder**. Concurrently, two through space paths can also be considered (path C + path F)_n and (path D + path E)_n. While the former path is hampered by smaller averaged κ^2/r^6 ratios the second pattern exhibits favorable ones (*i.e.* $> 1.92 \times 10^{-8} \text{ \AA}^{-6}$). However, both paths suffer from an unfavorable zig-zagging geometry for energy delocalization, the linear geometry being far more favored in Forster's theory.⁹⁴⁻⁹⁶

Considering now only linear paths in the 3 directions of the crystal indicated by the broken lines in **Figure 11**, the interchain Zn...Zn distances range from 16 to 20 Å. Such distances are much longer than for the intrachain ones (~10.0 to 15.3 Å; **Table 4**). Because of the $1/r^6$ relationship with the rate of energy transfer, *i.e.* $1/r^6 \propto k_{ET}$, interchain exciton energy migrations are predicted to be extremely slow (essentially negligible). In all, **1D Ladder** shows no evidence of singlet-singlet annihilation (*i.e.* no significant exciton energy migration), dictated by the structure of **1D ladder**, Forster's theory explaining the relative inefficiency of the exciton migration.

2D Grid and Morph

During this investigation a new structure of ZnTPyP (**2D Grid** = [ZnTPyP·4CHCl₃]_n) was crystallized and identified (**Figure 12** and **Table S10**). Its structure is a 2D array, which differs from that illustrated in **Figure 1d**.^{22,24} The key feature is the dislocation of the pyridine-Zn coordination. The N-Zn separation in **2D Grid** is 2.447(15) Å, while the coordination bond in **3D Helix** is 2.358 (7) Å. Concurrently, the angle formed by the pyridine plane and the N-Zn axis are 153.15 (8)° and 171.26 (15)°, for **2D Grid** and **3D Helix**, respectively. However, the crystals are unstable due to evaporation of the chloroform molecules, thus triggering a change in the network structure (**Figure S11**). In fact, this phase transformation led to a mixture of MOCNs, labelled **Morph**. Because of this instability, the photophysical properties were not assessed. After complete evolution of **2D Grid**, the resulting PXRD pattern of **Morph** was examined in an attempt to identify the new phases (**Figure 13**). The best combination where most scatterings are explained turned to be the **3D Helix** and two of the 1D-MOCNs listed in **Figure 1**. This outcome is not statistically surprising since 7 variations of the **3D Helix** structure (excluding this one herein),^{69,72,77-81} and 9 structures of various 1D-coordination polymers (1D single zig-zag,^{69,70} 1D double zig-zag^{69,71,72} and 1D ladder^{70,73-75} motifs) are known, compared to the 2D grids (2 structures),^{72,76} reported so far.. The relative amount of each phase is unknown.

The photophysical study with regards to exciton energy migration in **3D Helix** and **1D Ladder** indicated that the 3D structure is prone to efficient migration across the bulk whereas **1D Ladder** was not, stressing the fact that a zig-zag pattern was not favorable for such a process. In the mixture **Morph**, only the 3D Helix phase is predicted to perform exciton migration and singlet-singlet annihilation. However, this phase is *diluted* and this effect should be diminished.

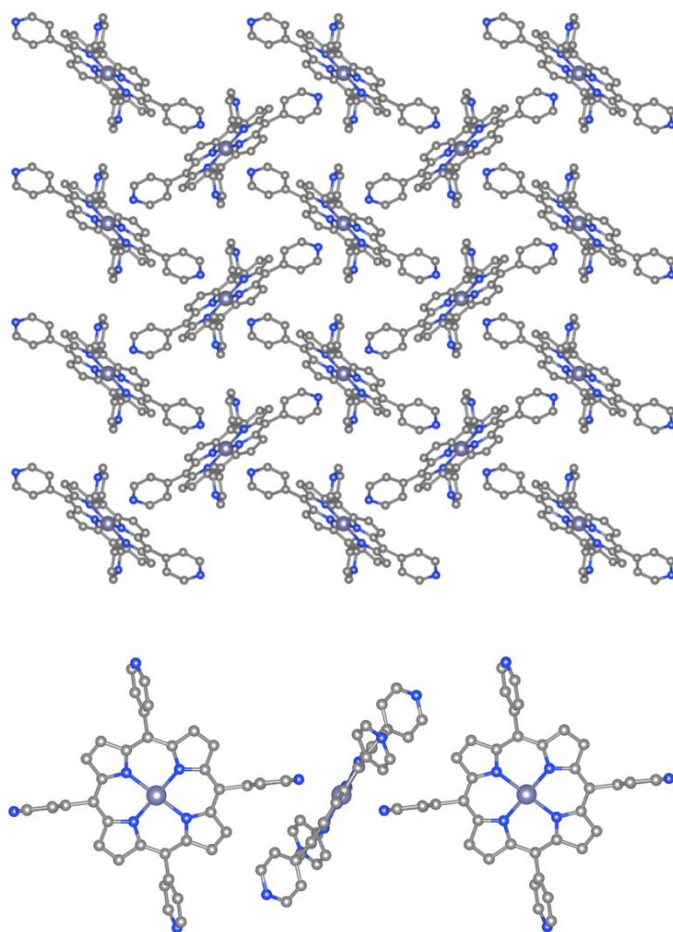


Figure 12: Elucidated structure of **2D Grid**. Note the unusual axial coordination angles (bottom) which make an overall “parallelogram”-type grid, contrasting with other “square”-type grids previously reported.^{72,76} These angles certainly contribute to the low observed stability of the structure. Solvent molecules and hydrogen atoms have been omitted for clarity.

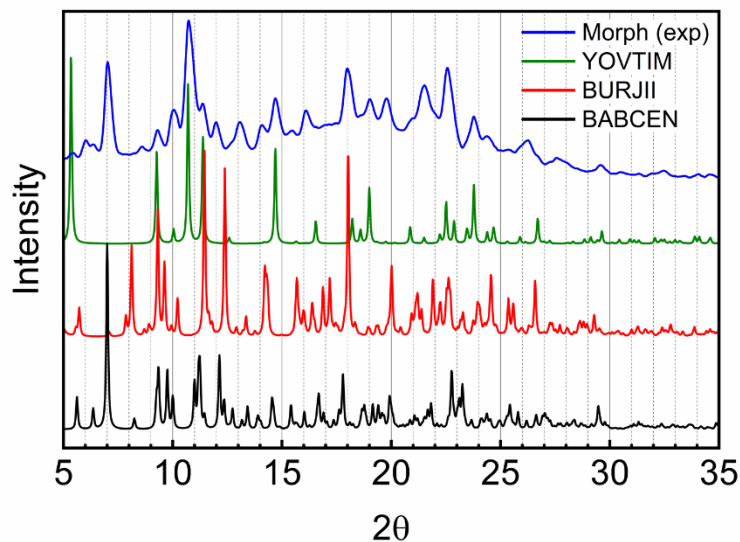


Figure 13: Comparison of the experimental PXR D pattern of **Morph** with simulated patterns of a **3D Helix** (YOVTIM),⁸¹ and two 1D ladder-type structures (BABCEN⁹³ and BURJII⁷⁰). The three identifiers are of the Cambridge Crystallographic Data Center (CCDC).

The photophysical data is presented in **Figures S12-S14**, and a brief account of the observations is provided: The mixture is weakly emissive, with two fluorescence lifetimes detected by TCSPC (~ 560 and ~ 20 ps) and four components using a Streak camera on a fs laser system (440, 104, 23 and 6 ps). The presence of several components is consistent with the multiphasic nature of the mixture. Concurrently at both 77 and 298K, the total fluorescence intensity increases linearly with the excitation power at low photon flux but the graph curves somewhat at high flux. Concurrently, the graph reporting the total fluorescence intensity versus $(\text{Power})^{1/2}$ is not linear at low power but becomes linear at high excitation power. The behaviour is consistent with absence of singlet-singlet annihilation due to the presence of a portion of 1D-coordination species and consequently exciton energy migration, but at high flux the small contribution of a *diluted 3D Helix* phase becomes more apparent. All in all, these measurements

performed on a mixture reinforce the conclusion that exciton energy migration in **3D Helix** network is more efficient than in **1D Ladder**.

Photosensitization of singlet oxygen

The ability of porphyrin and metalloporphyrin networks to photosensitize singlet oxygen ($^1\text{O}_2$) is well known, and various heterogeneous photocatalytic applications in photodynamic therapy, antibacterial processes, eradication of pollutants and toxins in water, and in organic synthesis have emerged in recent years.^{18–21} The photosensitizing ability is bound to depend on the efficiency of excitation energy delocalization across the bulk. The powders were pressed onto a glass plate and were excited in the Soret band at 444 nm (details in **Figure S15**). To confirm the nature of $^1\text{O}_2$ phosphorescence, the measurements were performed in air, argon, and pure oxygen atmospheres (raw spectra in **Figure S16**, and after corrections in **Figure 14**). Indeed, $^1\text{O}_2$ phosphorescence is observed at 1280 nm, which compares favorably to the signal often observed in solution (1275 nm).^{97,98} The slight shift in peak intensity wavelengths can be rationalized by extending the influence a solvent can have on the exact position of a band maximum to the gaseous environment.^{99–101} The maximal $^1\text{O}_2$ signal is reached when an atmosphere of pure oxygen is used. The key takeaway is that, qualitatively, the signal intensity is larger for **3D Helix** (~6000 cps) compared to **1D Ladder** (~600 cps) and the signal from **1D Ladder** is significantly noisier than that from **3D Helix**. In brief, **3D Helix** photosensitizes more $^1\text{O}_2$ than that of **1D Ladder**, which in absence of exciton migration, ends up wasting more energy through non-radiative deactivation processes.

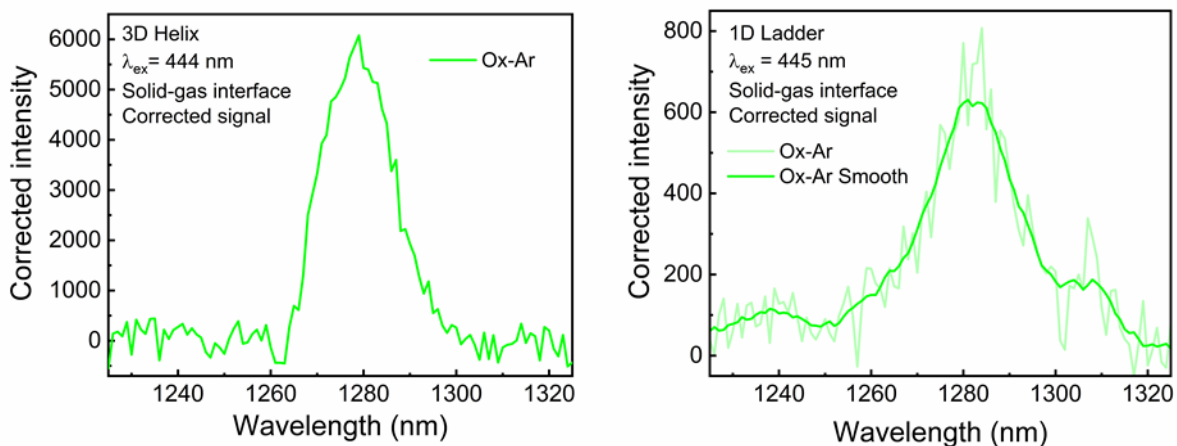


Figure 14: Phosphorescence of $^1\text{O}_2$ at the solid-gas interface of **3D Helix** (left, peak centered at ~ 1280 nm is an artifact) and **1D Ladder** (right). The signals are baseline corrected, and argon signal has been subtracted from the pure oxygen signal. Raw signals in **Figure S16**.

Conclusion

This investigation stressed on the structure-property relationship of two different auto-assembled MOCNs; a 3D network and a 1D coordination polymer using the same ligand ZnTPyP. These properties were excitation energy migration through singlet-singlet annihilation processes and photosensitization of $^1\text{O}_2$. The results indicated clearly that the 3D network was more prone to exciton migration and consequently was also more prone to generate $^1\text{O}_2$ when compared to the 1D coordination polymer, where no efficient exciton migration occurred. This demonstration of a direct link between excitation migration and photosensitization of $^1\text{O}_2$, is to the best of our knowledge, unprecedented. These findings hold a tremendous potential, particularly in fields involving reactive oxygen species (ROS) such as those enumerated above.^{18–21} First, the design of such photocatalysts would benefit from more widespread use of 3D structures, while 2D-, 1D-, and 0D species would probably be better suited for other uses.

Moreover, attention should be focused on providing linear paths and desirable structural parameters (*i.e.* κ^2/r^6). The photosensitization of $^1\text{O}_2$ *at the solid-gas interface* has not been widely studied in the scientific literature, but it is a key process to unlock access to $^1\text{O}_2$ from the most abundant source that is the atmosphere, for such applications as sanitary bandages^{102,103} or food packaging.^{104–106} It is also interesting to note that a simple measurement of $^1\text{O}_2$ phosphorescence intensity at the solid-gas interface allows a rapid, direct and reliable comparison of entire families of widely varied photosensitizers.

ASSOCIATED CONTENT

Electronic Supporting Information containing further structural and photophysical characterization data (NMR, IR, TGA, Elemental analyses, structural elucidations), full FRET analysis tables, DFT computation results, and singlet oxygen experimental setup details is available free of charge at <https://pubs.acs.org>.

CIF files for the structures of **3D Helix** and **2D Grid** have been deposited in the CCDC under identifiers #XYZ and #XYZ respectively. This data is available free of charge via <https://www.ccdc.cam.ac.uk/>, or by contacting the Cambridge Crystallographic Data Centre, 12 Union Road, Cambridge, CB2 1EZ, UK; fax: +44 1223 336033.

AUTHOR INFORMATION

Corresponding Author

* Please address correspondence to Pr. Pierre D. Harvey (Pierre.Harvey@USherbrooke.ca)

Author Contributions

The manuscript was written through contributions of all authors: P.A: Synthesis of ligands and MOCNs, structural characterization, photophysical measurements, data treatment and interpretation, figure creation, literature review, manuscript writing and proof-reading. A.S: Photophysical measurements, figure creation, literature review, manuscript proof-reading; D.F: Crystalline structural elucidation of **3D Helix** and **1D Ladder**, PXRD measurements; P-L. K: Power-dependence measurements on **3D Helix**, **1D Ladder**, and **Morph**, associated data pre-treatment; P. D. H: Literature review, data treatment, and interpretation, figure creation, manuscript writing and proof-reading. All authors have approved the final version of the manuscript.

Funding Sources

This work was supported by the Canadian Natural Sciences and Engineering Research Council (NSERC/CRSNG, grant RGPIN-2019-05289) and the *Fonds de Recherche du Québec – Nature et Technologies* (FRQNT). P. Asselin thanks both funding agencies for undergraduate scholarship grants #472729 and #279108.

Notes

All authors declare no conflicts of interest.

ACKNOWLEDGMENT

Dr. Adam Langlois is thanked for his technical insight in troubleshooting lifetime measurements.

Mr. Kevin Tanner is thanked for his assistance in setting up DFT computations.

REFERENCES

- (1) Kırbıyık, Ç.; Kuş, M. Advanced Applications of Green Materials for Gas Separation and Storage. In *Applications of Advanced Green Materials*; Elsevier, 2021; pp 681–703. <https://doi.org/10.1016/B978-0-12-820484-9.00026-X>.
- (2) Abdul Hamid, M. R.; Qian, Y.; Wei, R.; Li, Z.; Pan, Y.; Lai, Z.; Jeong, H.-K. Polycrystalline Metal-Organic Framework (MOF) Membranes for Molecular Separations: Engineering Prospects and Challenges. *J. Memb. Sci.* **2021**, *640*, 119802. <https://doi.org/10.1016/j.memsci.2021.119802>.
- (3) Shamim, M. A.; Zia, H.; Zeeshan, M.; Khan, M. Y.; Shahid, M. Metal Organic Frameworks (MOFs) as a Cutting-Edge Tool for the Selective Detection and Rapid Removal of Heavy Metal Ions from Water: Recent Progress. *J. Environ. Chem. Eng.* **2022**, *10* (1), 106991. <https://doi.org/10.1016/j.jece.2021.106991>.
- (4) Hooriabad Saboor, F.; Nasirpour, N.; Shahsavari, S.; Kazemian, H. The Effectiveness of MOFs for the Removal of Pharmaceuticals from Aquatic Environments: A Review Focused on Antibiotics Removal. *Chem. – An Asian J.* **2022**, *17* (4). <https://doi.org/10.1002/asia.202101105>.
- (5) Sharma, V. K.; Feng, M. Water Depollution Using Metal-Organic Frameworks-Catalyzed Advanced Oxidation Processes: A Review. *J. Hazard. Mater.* **2019**, *372*, 3–16. <https://doi.org/10.1016/j.jhazmat.2017.09.043>.
- (6) Yoon, J.; Kim, J.; Kim, C.; Jang, H. W.; Lee, J. MOF-Based Hybrids for Solar Fuel Production. *Adv. Energy Mater.* **2021**, *11* (27), 2003052. <https://doi.org/10.1002/aenm.202003052>.

- (7) Chuhadiya, S.; Himanshu; Suthar, D.; Patel, S. L.; Dhaka, M. S. Metal Organic Frameworks as Hybrid Porous Materials for Energy Storage and Conversion Devices: A Review. *Coord. Chem. Rev.* **2021**, *446*, 214115. <https://doi.org/10.1016/j.ccr.2021.214115>.
- (8) Wang, Q.; Astruc, D. State of the Art and Prospects in Metal–Organic Framework (MOF)-Based and MOF-Derived Nanocatalysis. *Chem. Rev.* **2020**, *120* (2), 1438–1511. <https://doi.org/10.1021/acs.chemrev.9b00223>.
- (9) Pettinari, C.; Pettinari, R.; Di Nicola, C.; Tombesi, A.; Scuri, S.; Marchetti, F. Antimicrobial MOFs. *Coord. Chem. Rev.* **2021**, *446*, 214121. <https://doi.org/10.1016/j.ccr.2021.214121>.
- (10) Sultana, A.; Kathuria, A.; Gaikwad, K. K. Metal–Organic Frameworks for Active Food Packaging. A Review. *Environ. Chem. Lett.* **2022**, *20* (2), 1479–1495. <https://doi.org/10.1007/s10311-022-01387-z>.
- (11) Alves, S. R.; Calori, I. R.; Tedesco, A. C. Photosensitizer-Based Metal-Organic Frameworks for Highly Effective Photodynamic Therapy. *Mater. Sci. Eng. C* **2021**, *131*, 112514. <https://doi.org/10.1016/j.msec.2021.112514>.
- (12) Mollick, S.; Fajal, S.; Mukherjee, S.; Ghosh, S. K. Stabilizing Metal–Organic Polyhedra (MOP): Issues and Strategies. *Chem. – An Asian J.* **2019**, *14* (18), 3096–3108. <https://doi.org/10.1002/asia.201900800>.
- (13) Baker Cortés, B. D.; Schmidt, N.; Enache, M.; Stöhr, M. Comparing Cyanophenyl and Pyridyl Ligands in the Formation of Porphyrin-Based Metal–Organic Coordination

- Networks. *J. Phys. Chem. C* **2021**, *125* (44), 24557–24567. <https://doi.org/10.1021/acs.jpcc.1c05360>.
- (14) Shi, Z.; Lin, N. Structural and Chemical Control in Assembly of Multicomponent Metal–Organic Coordination Networks on a Surface. *J. Am. Chem. Soc.* **2010**, *132* (31), 10756–10761. <https://doi.org/10.1021/ja1018578>.
- (15) Baker Cortés, B. D.; Enache, M.; Küster, K.; Studener, F.; Lee, T.; Marets, N.; Bulach, V.; Hosseini, M. W.; Stöhr, M. Structural Transformation of Surface-Confined Porphyrin Networks by Addition of Co Atoms. *Chem. – A Eur. J.* **2021**, *27* (48), 12430–12436. <https://doi.org/10.1002/chem.202101217>.
- (16) Bischoff, F.; He, Y.; Seufert, K.; Stassen, D.; Bonifazi, D.; Barth, J. V.; Auwärter, W. Tailoring Large Pores of Porphyrin Networks on Ag(111) by Metal–Organic Coordination. *Chem. - A Eur. J.* **2016**, *22* (43), 15298–15306. <https://doi.org/10.1002/chem.201602154>.
- (17) Laokroekkiat, S.; Hara, M.; Nagano, S.; Nagao, Y. Metal–Organic Coordination Network Thin Film by Surface-Induced Assembly. *Langmuir* **2016**, *32* (26), 6648–6655. <https://doi.org/10.1021/acs.langmuir.6b01251>.
- (18) Harvey, P. D. Porphyrin-Based MOFs as Heterogeneous Photocatalysts for the Eradication of Organic Pollutants and Toxins. *J. Porphyr. Phthalocyanines* **2021**, *25* (07n08), 583–604. <https://doi.org/10.1142/S1088424621300020>.
- (19) Schlachter, A.; Asselin, P.; Harvey, P. D. Porphyrin-Containing MOFs and COFs as Heterogeneous Photosensitizers for Singlet Oxygen-Based Antimicrobial Nanodevices. *ACS Appl. Mater. Interfaces* **2021**, *13* (23), 26651–26672.

<https://doi.org/10.1021/acsami.1c05234>.

- (20) Harvey, P. D. Porphyrin-Based Metal- and Covalent-Organic Frameworks as Heterogeneous Nanosized Photocatalysts in Organic Synthesis. *J. Mater. Chem. C* **2021**, *9* (47), 16885–16910. <https://doi.org/10.1039/D1TC04147A>.
- (21) Harvey, P. D.; Plé, J. Recent Advances in Nanoscale Metal–Organic Frameworks Towards Cancer Cell Cytotoxicity: An Overview. *J. Inorg. Organomet. Polym. Mater.* **2021**, *31* (7), 2715–2756. <https://doi.org/10.1007/s10904-021-02011-3>.
- (22) Wang, J.; He, W.-L.; Chen, M.; Qian, D.-J. Fabrication of Carbon Nanotube-Multiporphyrin Array Composites as Light-Sensitizer for Photocurrent Generation, Photochromism of Viologen and Catalytic Degradation of Methyl Orange. *New J. Chem.* **2018**, *42* (21), 17216–17226. <https://doi.org/10.1039/C8NJ03780A>.
- (23) Sun, Y.; Yoo, B. Morphological Transformation Reactions of Photocatalytic Metalloporphyrin-Containing Coordination Polymer Particles from Seed Structures. *ChemistryOpen* **2015**, *4* (4), 438–442. <https://doi.org/10.1002/open.201500076>.
- (24) Lu, Q.; Zhang, Y.; Liu, S. Graphene Quantum Dots Enhanced Photocatalytic Activity of Zinc Porphyrin toward the Degradation of Methylene Blue under Visible-Light Irradiation. *J. Mater. Chem. A* **2015**, *3* (16), 8552–8558. <https://doi.org/10.1039/C5TA00525F>.
- (25) Sun, Y.; Yoo, B. Monitoring the Length-Controlled Synthesis of One-Dimensional Metalloporphyrin-Containing Coordination Polymer Particles and Their Photocatalytic Properties. *New J. Chem.* **2015**, *39* (6), 4218–4221. <https://doi.org/10.1039/C5NJ00403A>.

- (26) Zhang, Z.; Li, X. Photocatalytic Degradation of Toluene Over Spindle-like Porphyrinoid Nanostructures. *Procedia Environ. Sci.* **2013**, *18*, 353–358. <https://doi.org/10.1016/j.proenv.2013.04.046>.
- (27) Guo, P.; Chen, P.; Liu, M. One-Dimensional Porphyrin Nanoassemblies Assisted via Graphene Oxide: Sheetlike Functional Surfactant and Enhanced Photocatalytic Behaviors. *ACS Appl. Mater. Interfaces* **2013**, *5* (11), 5336–5345. <https://doi.org/10.1021/am401260n>.
- (28) Cai, Y.-Q.; Ren, X.-B.; Wang, H.-L.; Huang, H.-X.; Chen, M.; Qian, D.-J. Pd(II)-Directed Layer-by-Layer Assembly and Characterization of Zinc Tetrapyrrolylporphyrin-Linked Poly(4-Vinylpyridine) Multilayers on Substrate Surfaces. *Synth. Met.* **2012**, *162* (21–22), 1871–1878. <https://doi.org/10.1016/j.synthmet.2012.09.002>.
- (29) Zhang, Z.; Tong, J.; Meng, X.; Cai, Y.; Ma, S.; Huo, F.; Luo, J.; Xu, B.-H.; Zhang, S.; Pinelo, M. Development of an Ionic Porphyrin-Based Platform as a Biomimetic Light-Harvesting Agent for High-Performance Photoenzymatic Synthesis of Methanol from CO₂. *ACS Sustain. Chem. Eng.* **2021**, *9* (34), 11503–11511. <https://doi.org/10.1021/acssuschemeng.1c03737>.
- (30) Łapok, Ł.; Schnurpfeil, G.; Gerdes, R.; Gorun, S. M.; Suvorova, O.; Kudryavtseva, G. S.; Wöhrle, D. Synthesis of Charged Triazatetrabenzcorroles, Phthalocyanines and Tetrapyrrolylporphyrin, and Their Activities in the Co-Sensitized Photooxidation of 2-Mercaptoethanol. *J. Porphyr. Phthalocyanines* **2009**, *13* (03), 346–357. <https://doi.org/10.1142/S1088424609000097>.
- (31) Giannoudis, E.; Benazzi, E.; Karlsson, J.; Copley, G.; Panagiotakis, S.; Landrou, G.;

- Angaridis, P.; Nikolaou, V.; Matthaiaki, C.; Charalambidis, G.; et al. Photosensitizers for H₂ Evolution Based on Charged or Neutral Zn and Sn Porphyrins. *Inorg. Chem.* **2020**, *59* (3), 1611–1621. <https://doi.org/10.1021/acs.inorgchem.9b01838>.
- (32) Natali, M.; Luisa, A.; Iengo, E.; Scandola, F. Efficient Photocatalytic Hydrogen Generation from Water by a Cationic Cobalt(II) Porphyrin. *Chem. Commun.* **2014**, *50* (15), 1842. <https://doi.org/10.1039/c3cc48882a>.
- (33) Shehata, M. M.; Kamal, H.; Abdelhady, K. Photovoltaic Performance, Structural and Electrical Characterizations of Thermally Evaporated 5,10,15,20-Tetra(4-Pyridyl)-21H,23H-Prophine Zinc (ZnTPyP) Organic Thin Films. *Vacuum* **2018**, *154*, 129–140. <https://doi.org/10.1016/j.vacuum.2018.05.001>.
- (34) Shehata, M. M.; Abdel-Malik, T. G.; Abdelhady, K. AC Impedance Spectroscopy on Al/p-Si/ZnTPyP/Au Heterojunction for Hybrid Solar Cell Applications. *J. Alloys Compd.* **2018**, *736*, 225–235. <https://doi.org/10.1016/j.jallcom.2017.11.097>.
- (35) Deng, W.-T.; Liu, J.-C.; Cao, J.; Hu, D.-C.; Li, R.-Z.; Jin, N.-Z. Design and Fabrication of a Series of Metal-Mediated Assemblies with Tetrapyrrolylporphyrins for Supramolecular Solar Cells. *Dalt. Trans.* **2014**, *43* (2), 626–631. <https://doi.org/10.1039/C3DT52129J>.
- (36) Vasilopoulou, M.; Georgiadou, D. G.; Douvas, A. M.; Soutati, A.; Constantoudis, V.; Davazoglou, D.; Gardelis, S.; Palilis, L. C.; Fakis, M.; Kennou, S.; et al. Porphyrin Oriented Self-Assembled Nanostructures for Efficient Exciton Dissociation in High-Performing Organic Photovoltaics. *J. Mater. Chem. A* **2014**, *2* (1), 182–192. <https://doi.org/10.1039/C3TA13107F>.

- (37) Cao, J.; Liu, J.-C.; Deng, W.-T.; Li, R.-Z.; Jin, N.-Z. Effect of a Novel Self-Assembly Based on Coordination Polymer with Zinc Porphyrin in Supramolecular Solar Cells. *Org. Electron.* **2013**, *14* (11), 2713–2720. <https://doi.org/10.1016/j.orgel.2013.07.033>.
- (38) Daphnomili, D.; Landrou, G.; Prakash Singh, S.; Thomas, A.; Yesudas, K.; K., B.; Sharma, G. D.; Coutsolelos, A. G. Photophysical, Electrochemical and Photovoltaic Properties of Dye Sensitized Solar Cells Using a Series of Pyridyl Functionalized Porphyrin Dyes. *RSC Adv.* **2012**, *2* (33), 12899. <https://doi.org/10.1039/c2ra22129b>.
- (39) Umeyama, T.; Mihara, J.; Tezuka, N.; Matano, Y.; Stranius, K.; Chukharev, V.; Tkachenko, N. V.; Lemmetyinen, H.; Noda, K.; Matsushige, K.; et al. Preparation and Photophysical and Photoelectrochemical Properties of a Covalently Fixed Porphyrin-Chemically Converted Graphene Composite. *Chem. - A Eur. J.* **2012**, *18* (14), 4250–4257. <https://doi.org/10.1002/chem.201103843>.
- (40) Hasobe, T.; Sandanayaka, A. S. D.; Wada, T.; Araki, Y. Fullerene-Encapsulated Porphyrin Hexagonal Nanorods. An Anisotropic Donor–Acceptor Composite for Efficient Photoinduced Electron Transfer and Light Energy Conversion. *Chem. Commun.* **2008**, No. 29, 3372. <https://doi.org/10.1039/b806748a>.
- (41) Wang, J.; Zhong, Y.; Wang, L.; Zhang, N.; Cao, R.; Bian, K.; Alarid, L.; Haddad, R. E.; Bai, F.; Fan, H. Morphology-Controlled Synthesis and Metalation of Porphyrin Nanoparticles with Enhanced Photocatalytic Performance. *Nano Lett.* **2016**, *16* (10), 6523–6528. <https://doi.org/10.1021/acs.nanolett.6b03135>.
- (42) Guo, P.; Chen, P.; Ma, W.; Liu, M. Morphology-Dependent Supramolecular Photocatalytic Performance of Porphyrin Nanoassemblies: From Molecule to Artificial

- Supramolecular Nanoantenna. *J. Mater. Chem.* **2012**, *22* (38), 20243.
<https://doi.org/10.1039/c2jm33253a>.
- (43) Li, D.-J.; Li, Q.; Wang, Z.-R.; Ma, Z.-Z.; Gu, Z.-G.; Zhang, J. Interpenetrated Metal-Porphyrinic Framework for Enhanced Nonlinear Optical Limiting. *J. Am. Chem. Soc.* **2021**, *143* (41), 17162–17169. <https://doi.org/10.1021/jacs.1c07803>.
- (44) Makhoulf, M. M.; Shehata, M. M. Impact of Zn²⁺ Introduced into the Central Cavity of Meso-Tetra(4-Pyridyl)Porphine on Its Spectroscopic Features. *Opt. Mater. (Amst)*. **2021**, *113*, 110893. <https://doi.org/10.1016/j.optmat.2021.110893>.
- (45) Gao, F.; Bai, L.; Liu, S.; Zhang, R.; Zhang, J.; Feng, X.; Zheng, Y.; Zhao, Y. Rationally Encapsulated Gold Nanorods Improving Both Linear and Nonlinear Photoacoustic Imaging Contrast in Vivo. *Nanoscale* **2017**, *9* (1), 79–86.
<https://doi.org/10.1039/C6NR07528B>.
- (46) Hosoyamada, M.; Yanai, N.; Okumura, K.; Uchihashi, T.; Kimizuka, N. Translating MOF Chemistry into Supramolecular Chemistry: Soluble Coordination Nanofibers Showing Efficient Photon Upconversion. *Chem. Commun.* **2018**, *54* (50), 6828–6831.
<https://doi.org/10.1039/C8CC01594E>.
- (47) Levin, P. P.; Costa, S. M. B. Photokinetics in Tetraphenylporphyrin – Molecular Oxygen System at Gas/Solid Interfaces: Effect of Singlet Oxygen Quenchers on Oxygen-Induced Delayed Fluorescence. *Chem. Phys.* **2001**, *263* (2–3), 423–436.
[https://doi.org/10.1016/S0301-0104\(00\)00365-7](https://doi.org/10.1016/S0301-0104(00)00365-7).
- (48) Khalil, G. E.; Chang, A.; Gouterman, M.; Callis, J. B.; Dalton, L. R.; Turro, N. J.;

- Jockusch, S. Oxygen Pressure Measurement Using Singlet Oxygen Emission. *Rev. Sci. Instrum.* **2005**, *76* (5), 054101. <https://doi.org/10.1063/1.1896623>.
- (49) Matrosova, O. V.; Rufov, Y. N.; Vishnetskaya, M. V. Low-Temperature Emission of Singlet Oxygen from the Surface of Transition Metal Oxides. *Russ. J. Phys. Chem. A* **2010**, *84* (12), 2187–2189. <https://doi.org/10.1134/S0036024410120319>.
- (50) Sharma, N.; Dhankhar, S. S.; Nagaraja, C. M. Environment-Friendly, Co-Catalyst- and Solvent-Free Fixation of CO₂ Using an Ionic Zinc(II)–Porphyrin Complex Immobilized in Porous Metal–Organic Frameworks. *Sustain. Energy Fuels* **2019**, *3* (11), 2977–2982. <https://doi.org/10.1039/C9SE00282K>.
- (51) Frisch, M. J. et al. Gaussian 16. Gaussian Inc. 2016.
- (52) Hohenberg, P.; Kohn, W. Inhomogeneous Electron Gas. *Phys. Rev.* **1964**, *136* (3B), B864–B871. <https://doi.org/10.1103/PhysRev.136.B864>.
- (53) Kohn, W.; Sham, L. J. Self-Consistent Equations Including Exchange and Correlation Effects. *Phys. Rev.* **1965**, *140* (4A), A1133–A1138. <https://doi.org/10.1103/PhysRev.140.A1133>.
- (54) Parr, R. G.; Yang, W. Density Functional Theory of Atoms and Molecules. *Oxford Univ. Press* **1989**.
- (55) *The Challenge of d and f Electrons*; Salahub, D. R., Zerner, M. C., Eds.; ACS Symposium Series; American Chemical Society: Washington, DC, 1989; Vol. 394. <https://doi.org/10.1021/bk-1989-0394>.
- (56) Bauernschmitt, R.; Ahlrichs, R. Treatment of Electronic Excitations within the Adiabatic

- Approximation of Time Dependent Density Functional Theory. *Chem. Phys. Lett.* **1996**, 256 (4–5), 454–464. [https://doi.org/10.1016/0009-2614\(96\)00440-X](https://doi.org/10.1016/0009-2614(96)00440-X).
- (57) Casida, M. E.; Jamorski, C.; Casida, K. C.; Salahub, D. R. Molecular Excitation Energies to High-Lying Bound States from Time-Dependent Density-Functional Response Theory: Characterization and Correction of the Time-Dependent Local Density Approximation Ionization Threshold. *J. Chem. Phys.* **1998**, 108 (11), 4439–4449. <https://doi.org/10.1063/1.475855>.
- (58) Stratmann, R. E.; Scuseria, G. E.; Frisch, M. J. An Efficient Implementation of Time-Dependent Density-Functional Theory for the Calculation of Excitation Energies of Large Molecules. *J. Chem. Phys.* **1998**, 109 (19), 8218–8224. <https://doi.org/10.1063/1.477483>.
- (59) Lee, C.; Yang, W.; Parr, R. G. Development of the Colle-Salvetti Correlation-Energy Formula into a Functional of the Electron Density. *Phys. Rev. B* **1988**, 37 (2), 785–789. <https://doi.org/10.1103/PhysRevB.37.785>.
- (60) Miehlich, B.; Savin, A.; Stoll, H.; Preuss, H. Results Obtained with the Correlation Energy Density Functionals of Becke and Lee, Yang and Parr. *Chem. Phys. Lett.* **1989**, 157 (3), 200–206. [https://doi.org/10.1016/0009-2614\(89\)87234-3](https://doi.org/10.1016/0009-2614(89)87234-3).
- (61) Becke, A. D. Density-functional Thermochemistry. III. The Role of Exact Exchange. *J. Chem. Phys.* **1993**, 98 (7), 5648–5652. <https://doi.org/10.1063/1.464913>.
- (62) Binkley, J. S.; Pople, J. A.; Hehre, W. J. Self-Consistent Molecular Orbital Methods. 21. Small Split-Valence Basis Sets for First-Row Elements. *J. Am. Chem. Soc.* **1980**, 102 (3), 939–947. <https://doi.org/10.1021/ja00523a008>.

- (63) Gordon, M. S.; Binkley, J. S.; Pople, J. A.; Pietro, W. J.; Hehre, W. J. Self-Consistent Molecular-Orbital Methods. 22. Small Split-Valence Basis Sets for Second-Row Elements. *J. Am. Chem. Soc.* **1982**, *104* (10), 2797–2803. <https://doi.org/10.1021/ja00374a017>.
- (64) Pietro, W. J.; Francl, M. M.; Hehre, W. J.; DeFrees, D. J.; Pople, J. A.; Binkley, J. S. Self-Consistent Molecular Orbital Methods. 24. Supplemented Small Split-Valence Basis Sets for Second-Row Elements. *J. Am. Chem. Soc.* **1982**, *104* (19), 5039–5048. <https://doi.org/10.1021/ja00383a007>.
- (65) Dobbs, K. D.; Hehre, W. J. Molecular Orbital Theory of the Properties of Inorganic and Organometallic Compounds 4. Extended Basis Sets for Third-and Fourth-Row, Main-Group Elements. *J. Comput. Chem.* **1986**, *7* (3), 359–378. <https://doi.org/10.1002/jcc.540070313>.
- (66) Dobbs, K. D.; Hehre, W. J. Molecular Orbital Theory of the Properties of Inorganic and Organometallic Compounds 5. Extended Basis Sets for First-Row Transition Metals. *J. Comput. Chem.* **1987**, *8* (6), 861–879. <https://doi.org/10.1002/jcc.540080614>.
- (67) Dobbs, K. D.; Hehre, W. J. Molecular Orbital Theory of the Properties of Inorganic and Organometallic Compounds. 6. Extended Basis Sets for Second-Row Transition Metals. *J. Comput. Chem.* **1987**, *8* (6), 880–893. <https://doi.org/10.1002/jcc.540080615>.
- (68) O'boyle, N. M.; Tenderholt, A. L.; Langner, K. M. Cclib: A Library for Package-Independent Computational Chemistry Algorithms. *J. Comput. Chem.* **2008**, *29* (5), 839–845. <https://doi.org/10.1002/jcc.20823>.

- (69) Shi, Z.; Lin, N. Structural and Chemical Control in Assembly of Multicomponent Metal–Organic Coordination Networks on a Surface. *J. Am. Chem. Soc.* **2010**, *132* (31), 10756–10761. <https://doi.org/10.1021/ja1018578>.
- (70) Seidel, R. W.; Goddard, R.; Föcker, K.; Oppel, I. M. Supramolecular Isomerism of Self-Complementary Zinc-5,10,15,20-Tetra(4-Pyridyl)Porphyrin in the Presence of Dimethylformamide. *CrystEngComm* **2010**, *12* (2), 387–394. <https://doi.org/10.1039/B913791B>.
- (71) Ring, D. J.; Aragoni, M. C.; Champness, N. R.; Wilson, C. A Coordination Polymer Supramolecular Isomer Formed from a Single Building Block: An Unexpected Porphyrin Ribbon Constructed from Zinc(Tetra(4-Pyridyl)Porphyrin). *CrystEngComm* **2005**, *7*, 621–623.
- (72) Deiters, E.; Bulach, V.; Hosseini, M. W. Reversible Single-Crystal-to-Single-Crystal Guest Exchange in a 3-D Coordination Network Based on a Zinc Porphyrin. *Chem. Commun* **2005**, 3906–3908.
- (73) Koner, R.; Goldberg, I. Square-Grid Coordination Networks of (5,10,15,20-Tetra-4-Pyridylporphyrin-ato)Zinc(II) in Its Clathrate with Two Guest Molecules of 1,2-Dichloro-benzene: Supra-molecular Isomerism of the Porphyrin Self-Assembly. *Acta Crystallogr. Sect. C Cryst. Struct. Commun.* **2009**, *C65*, m139–m142.
- (74) Hu, J. S.; Guo, Y. G.; Liang, H. P.; Wan, L. J.; Jiang, L. Three-Dimensional Self-Organization of Supramolecular Self-Assembled Porphyrin Hollow Hexagonal Nanoprisms. *J. Am. Chem. Soc.* **2005**, *127* (48), 17090–17095. <https://doi.org/10.1021/ja0553912>.

- (75) Diskin-Posner, Y.; Patra, G. K.; Goldberg, I. Supramolecular Assembly of Metalloporphyrins in Crystals by Axial Coordination through Amine Ligands. *J. Chem. Soc. Dalt. Trans.* **2001**, 2 (19), 2775–2782. <https://doi.org/10.1039/b104961p>.
- (76) Makiura, R.; Konovalov, O. Bottom-up Assembly of Ultrathin Sub-Micron Size Metal-Organic Framework Sheets. *Dalt. Trans.* **2013**, 42 (45), 15931–15936. <https://doi.org/10.1039/c3dt51703a>.
- (77) Koner, R.; Goldberg, I. Heteromolecular Grids of Free-Base and Zinc-Tetra(4-Pyridyl)Porphyrins with Benzenetetracarboxylic Acid. *J. Incl. Phenom. Macrocycl. Chem.* **2010**, 66 (3), 403–408. <https://doi.org/10.1007/s10847-009-9611-0>.
- (78) Bai, F.; Sun, Z.; Wu, H.; Haddad, R. E.; Coker, E. N.; Huang, J. Y.; Rodriguez, M. A.; Fan, H. Porous One-Dimensional Nanostructures through Confined Cooperative Self-Assembly. *Nano Lett* **2011**, 11 (12), 5196–5200.
- (79) Sun, W.; Wang, H.; Qi, D.; Wang, L.; Wang, K.; Kan, J.; Li, W.; Chen, Y.; Jiang, J. 5,10,15,20-Tetra(4-Pyridyl)Porphyrinato Zinc Coordination Polymeric Particles with Different Shapes and Luminescent Properties. *CrystEngComm* **2012**, 14 (22), 7780–7786. <https://doi.org/10.1039/c2ce25187f>.
- (80) Lin, K.-J. SMTP-1: The First Functionalized Metalloporphyrin Molecular Sieves with Large Channels. *Angew. Chemie Int. Ed.* **1999**, 38 (18), 2730–2732. [https://doi.org/10.1002/\(SICI\)1521-3773\(19990917\)38:18<2730::AID-ANIE2730>3.0.CO;2-9](https://doi.org/10.1002/(SICI)1521-3773(19990917)38:18<2730::AID-ANIE2730>3.0.CO;2-9).
- (81) Krupitsky, H.; Stein, Z.; Goldberg, I.; Strouse, C. E. Crystalline Complexes, Coordination

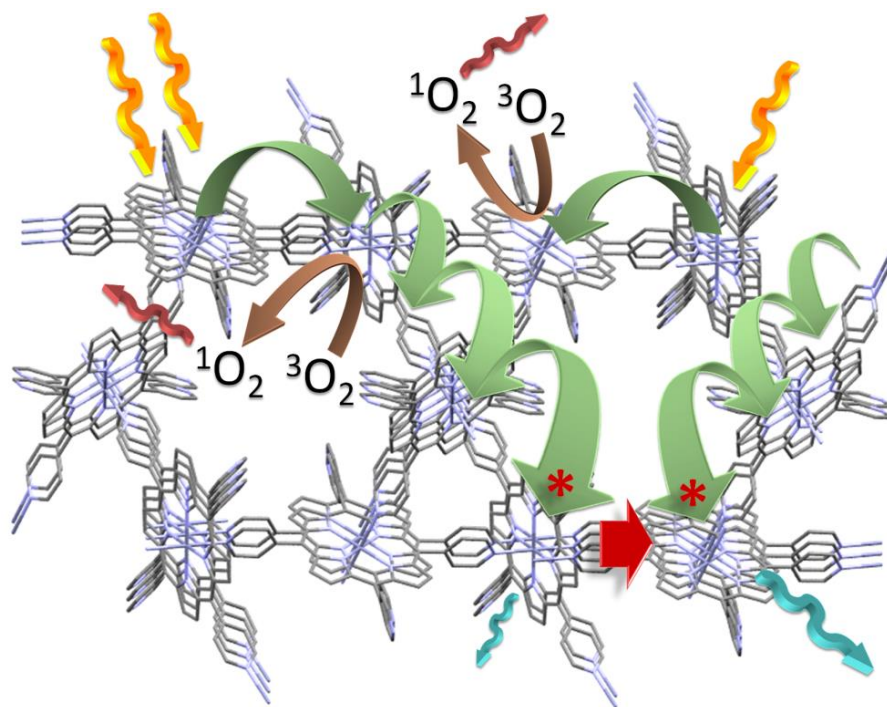
- Polymers and Aggregation Modes of Tetra(4-Pyridyl)Porphyrin. *J. Incl. Phenom. Mol. Recognit. Chem.* **1994**, *18* (2), 177–192. <https://doi.org/10.1007/BF00705820>.
- (82) Sun, W.; Wang, H.; Qi, D.; Wang, L.; Wang, K.; Kan, J.; Li, W.; Chen, Y.; Jiang, J. 5,10,15,20-Tetra(4-Pyridyl)Porphyrinato Zinc Coordination Polymeric Particles with Different Shapes and Luminescent Properties. *CrystEngComm* **2012**, *14* (22), 7780. <https://doi.org/10.1039/c2ce25187f>.
- (83) Ermakova, E. V.; Enakieva, Y. Y.; Nefedov, S. E.; Arslanov, V. V.; Gorbunova, Y. G.; Tsvadze, A. Y.; Stern, C.; Bessmertnykh-Lemeune, A. Synthesis of (Trans -A 2)BC-Type Porphyrins with Acceptor Diethoxyphosphoryl and Various Donor Groups and Their Assembling in the Solid State and at Interfaces. *European J. Org. Chem.* **2019**, *2019* (20), 3146–3162. <https://doi.org/10.1002/ejoc.201900448>.
- (84) Ermakova, E. V.; Ezhov, A. A.; Baranchikov, A. E.; Gorbunova, Y. G.; Kalinina, M. A.; Arslanov, V. V. Interfacial Self-Assembly of Functional Bilayer Templates Comprising Porphyrin Arrays and Graphene Oxide. *J. Colloid Interface Sci.* **2018**, *530*, 521–531. <https://doi.org/10.1016/j.jcis.2018.06.086>.
- (85) Bai, F.; Sun, Z.; Wu, H.; Haddad, R. E.; Coker, E. N.; Huang, J. Y.; Rodriguez, M. A.; Fan, H. Porous One-Dimensional Nanostructures through Confined Cooperative Self-Assembly. *Nano Lett.* **2011**, *11* (12), 5196–5200. <https://doi.org/10.1021/nl203598n>.
- (86) *Multiporphyrin Arrays, Fundamentals and Applications*; Kim, D., Ed.; CRC Press, 2012.
- (87) Prodi, A.; Indelli, M. T.; Kleverlaan, C. J.; Scandola, F.; Alessio, E.; Gianferrara, T.; Marzilli, L. G. Side-to-Face Ruthenium Porphyrin Arrays: Photophysical Behavior of

- Dimeric and Pentameric Systems. *Chem. - A Eur. J.* **1999**, *5* (9), 2668–2679.
[https://doi.org/10.1002/\(SICI\)1521-3765\(19990903\)5:9<2668::AID-CHEM2668>3.0.CO;2-M](https://doi.org/10.1002/(SICI)1521-3765(19990903)5:9<2668::AID-CHEM2668>3.0.CO;2-M).
- (88) Langlois, A.; Xu, H.-J.; Brizet, B.; Denat, F.; Brabe, J.-M.; Gros, C.; Harvey, P. D. Origin of Temperature Dependence of Rate of Singlet Energy Transfer in Three Component Truxene Bridged Dyad. *J. Porphyr. Phthalocyanines* **2014**, *18* (1–2), 94–106.
- (89) Langlois, A.; Harvey, P. D. Maple(TM)-Assisted Calculations of the J-Integral: A Key Parameter for the Understanding of Excited State Energy Transfer in Porphyrins and Other Chromophores. *J. Porphyr. Phthalocyanines* **2014**, *18* (8–9), 666–674.
- (90) Förster, T. Zwischenmolekulare Energiewanderung Und Fluoreszenz. *Ann. Phys.* **1948**, *6* (2), 55–75.
- (91) Förster, T. Energy Migration and Fluorescence. *J. Biomed. Opt.* **2012**, *17* (1), 011002.
<https://doi.org/10.1117/1.jbo.17.1.011002>.
- (92) Förster, T. Transfer Mechanisms of Electronic Excitation. In *10th Spiers Memorial Lecture*; 1959; pp 7–17.
- (93) Diskin-Posner, Y.; Patra, G. K.; Goldberg, I. Supramolecular Assembly of Metalloporphyrins in Crystals by Axial Coordination through Amine Ligands. *J. Chem. Soc. Dalt. Trans.* **2001**, No. 19, 2775–2782. <https://doi.org/10.1039/b104961p>.
- (94) Yanai, N.; Kimizuka, N. Recent Emergence of Photon Upconversion Based on Triplet Energy Migration in Molecular Assemblies. *Chem. Commun.* **2016**, *52* (31), 5354–5370.
<https://doi.org/10.1039/C6CC00089D>.

- (95) Andrew, T. L.; Swager, T. M. Structure-Property Relationships for Exciton Transfer in Conjugated Polymers. *J. Polym. Sci. Part B Polym. Phys.* **2011**, *49* (7), 476–498. <https://doi.org/10.1002/polb.22207>.
- (96) Yang, J.; Kim, D. Excitation Energy Migration Processes in Various Multi-Porphyrin Assemblies. *Philos. Trans. R. Soc. A Math. Phys. Eng. Sci.* **2012**, *370* (1972), 3802–3818. <https://doi.org/10.1098/rsta.2011.0206>.
- (97) Khan, A. U.; Kasha, M. Direct Spectroscopic Observation of Singlet Oxygen Emission at 1268 Nm Excited by Sensitizing Dyes of Biological Interest in Liquid Solution. *Proc. Natl. Acad. Sci.* **1979**, *76* (12), 6047–6049. <https://doi.org/10.1073/pnas.76.12.6047>.
- (98) Wessels, J. M.; Rodgers, M. A. J. Effect of Solvent Polarizability on the Forbidden $1\Delta_g \rightarrow 3\Sigma_g^-$ Transition in Molecular Oxygen: A Fourier Transform near-Infrared Luminescence Study. *J. Phys. Chem.* **1995**, *99* (49), 17586–17592. <https://doi.org/10.1021/j100049a019>.
- (99) Wessels, J. M.; Rodgers, M. A. J. Effect of Solvent Polarizability on the Forbidden $1\Delta_g \rightarrow 3\Sigma_g^-$ Transition in Molecular Oxygen: A Fourier Transform near-Infrared Luminescence Study. *J. Phys. Chem.* **1995**, *99* (49), 17586–17592. <https://doi.org/10.1021/j100049a019>.
- (100) Bregnhøj, M.; Westberg, M.; Minaev, B. F.; Ogilby, P. R. Singlet Oxygen Photophysics in Liquid Solvents: Converging on a Unified Picture. *Acc. Chem. Res.* **2017**, *50* (8), 1920–1927. <https://doi.org/10.1021/acs.accounts.7b00169>.
- (101) Ogilby, P. R. Solvent Effects on the Radiative Transitions of Singlet Oxygen. *Acc. Chem.*

Res. **1999**, 32 (6), 512–519. <https://doi.org/10.1021/ar980005p>.

- (102) Arenbergerova, M.; Arenberger, P.; Bednar, M.; Kubat, P.; Mosinger, J. Light-Activated Nanofibre Textiles Exert Antibacterial Effects in the Setting of Chronic Wound Healing. *Exp. Dermatol.* **2012**, 21 (8), 619–624. <https://doi.org/10.1111/j.1600-0625.2012.01536.x>.
- (103) Kammerlander, G.; Assadian, O.; Eberlein, T.; Zweitmuller, P.; Luchsinger, S.; Andriessen, A. A Clinical Evaluation of the Efficacy and Safety of Singlet Oxygen in Cleansing and Disinfecting Stagnating Wounds. *J. Wound Care* **2011**, 20 (4), 149–158. <https://doi.org/10.12968/jowc.2011.20.4.149>.
- (104) Cai, Y.; Guan, J.; Wang, W.; Wang, L.; Su, J.; Fang, L. PH and Light-responsive Polycaprolactone/Curcumin@zif-8 Composite Films with Enhanced Antibacterial Activity. *J. Food Sci.* **2021**, 86 (8), 3550–3562. <https://doi.org/10.1111/1750-3841.15839>.
- (105) Min, T.; Sun, X.; Zhou, L.; Du, H.; Zhu, Z.; Wen, Y. Electrospun Pullulan/PVA Nanofibers Integrated with Thymol-Loaded Porphyrin Metal–organic Framework for Antibacterial Food Packaging. *Carbohydr. Polym.* **2021**, 270, 118391. <https://doi.org/10.1016/j.carbpol.2021.118391>.
- (106) Su, L.; Huang, J.; Li, H.; Pan, Y.; Zhu, B.; Zhao, Y.; Liu, H. Chitosan-Riboflavin Composite Film Based on Photodynamic Inactivation Technology for Antibacterial Food Packaging. *Int. J. Biol. Macromol.* **2021**, 172, 231–240. <https://doi.org/10.1016/j.ijbiomac.2021.01.056>.



Graphic art